

Elsevier Editorial System(tm) for Ocean Modelling
Manuscript Draft

Manuscript Number:

Title: Turbulent flow regimes behind a coastal cape in a stratified and rotating environment

Article Type: Full Length Article

Corresponding Author: PhD Student Marcello Magaldi,

Corresponding Author's Institution: RSMAS, University of Miami

First Author: Marcello Magaldi

Order of Authors: Marcello Magaldi; Tamay M Ozgokmen; Annalisa Griffa; Eric P Chassignet; Mohamed Iskandarani; Hartmut Peters

Abstract: A numerical study aimed at investigating the roles of both the stratification and topographic slope in generation of turbulent coherent structures in the lee of capes is presented. We consider a steady barotropic current impinging on an obstacle in a rotating and linearly-stratified environment. The obstacle is a triangular prism and represents an idealized headland extending from the coast. Numerical experiments are conducted varying the Burger number, Bu , and the obstacle slope, α .

Flow regime diagrams in the Bu - α space are determined. For $Bu < 0.1$, vertical movement over the obstacle is enhanced and a fully-attached regime with pronounced internal waves is established. For $0.1 \leq Bu < 1$, fluid parcels flow more around the obstacle than over it. Flow separation occurs and small tip eddies start to shed. For $Bu \geq 1$, tip eddies merge to form larger eddies in the lee of the cape. We find that previous laboratory results cannot be used for gentler slopes, since bottom flow regimes are strongly dependent on α when $Bu \geq 1$.

The form drag coefficient exerted by the cape is at least two orders of

magnitude larger than the one due to skin friction. It increases with increasing Burger numbers and decreasing slopes. When no separation occurs (low Bu), the increase with decreasing slopes is the result of the mixing associated with hydraulic phenomena. For intermediate and high Bu , form drag coefficients reach larger values as a result of the boundary layer mixing associated with flow separation. We put forth an empirical parametrization of form drag in the Bu - α space.

Suggested Reviewers: Parker MacCready

Associate Professor, School of Oceanography, University of Washington

parker@ocean.washington.edu

expert this field

Jonathan Nash

Associate Professor, College of Oceanic and Atmospheric Sciences , Oregon State University

nash@coas.oregonstate.edu

expert in this field

Rocky Geyer

Senior Scientist, Applied Ocean Physics and Engineering , Woods Hole Oceanographic Institution

rgeyer@whoi.edu

expert in this field

Opposed Reviewers:

Marcello Magaldi
RSMAS/MPO
University of Miami
4600 Rickenbacker Causeway
Miami, FL 33149-1098
mmagaldi@rsmas.miami.edu

January 29, 2008

Chief Editor, *Ocean Modelling*

Dear Editor,

Enclosed herewith please find the manuscript entitled "*Turbulent flow regimes behind a coastal cape in a stratified rotating environment*", which we would like to submit for publication in *Ocean Modelling*.

This manuscript has not been published in any language and it is not under consideration for publication by another journal. All authors are aware of this submission.

Sincerely yours,

Marcello Magaldi
PhD Student in Physical
Oceanography

Turbulent flow regimes behind a coastal cape in a stratified and rotating environment

M. G. Magaldi^a, T. M. Özgökmen^a, A. Griffa^{a,b},
E. P. Chassignet^c, M. Iskandarani^a, H. Peters^a

^a*Rosenstiel School of Marine and Atmospheric Science/MPO, Univ. of Miami,
4600 Rickenbacker Cswy, Miami, Florida, 33149-1098, USA*

^b*Istituto delle Scienze Marine,
Consiglio Nazionale delle Ricerche, Sezione di Lerici,
Forte Santa Teresa, I-19036, Pozzuolo di Lerici (SP), Italy*

^c*Center for Ocean-Atmospheric Prediction Studies, Florida State University,
200 RM Johnson Bldg, Tallahassee, Florida, 32306-4320, USA*

Abstract

A numerical study aimed at investigating the roles of both the stratification and topographic slope in generation of turbulent coherent structures in the lee of capes is presented. We consider a steady barotropic current impinging on an obstacle in a rotating and linearly-stratified environment. The obstacle is a triangular prism and represents an idealized headland extending from the coast. Numerical experiments are conducted varying the Burger number, Bu , and the obstacle slope, α .

Flow regime diagrams in the $Bu - \alpha$ space are determined. For $Bu < 0.1$, vertical movement over the obstacle is enhanced and a fully-attached regime with pronounced internal waves is established. For $0.1 \leq Bu < 1$, fluid parcels flow more around the obstacle than over it. Flow separation occurs and small tip eddies start to shed. For $Bu \geq 1$, tip eddies merge to form larger eddies in the lee of the cape. We find that previous laboratory results cannot be used for gentler slopes, since bottom flow regimes are strongly dependent on α when $Bu \geq 1$.

The form drag coefficient exerted by the cape is at least two orders of magnitude larger than the one due to skin friction. It increases with increasing Burger numbers and decreasing slopes. When no separation occurs (low Bu), the increase with decreasing slopes is the result of the mixing associated with hydraulic phenomena. For intermediate and high Bu , form drag coefficients reach larger values as a result of the boundary layer mixing associated with flow separation. We put forth an empirical parametrization of form drag in the $Bu - \alpha$ space.

Key words: Cape; headland; eddy generation; modeling; form drag; mixing.

1 Introduction

Coastal circulation is influenced by the complex shape of the coastline. In particular, leeward eddies have been observed behind topographic features like prominent headlands and capes (e.g. Pattiaratchi et al., 1986; Farmer et al., 2002; McCabe et al., 2006). These eddies impact the physics of coastal systems and play a role in biological, ecological, and geological processes. Leeward eddies affect the dispersion of dissolved pollutants, floating organisms, nutrients and suspended sediments (Hayward and Mantyla, 1990).

From a dynamical perspective, capes and headlands are important for the circulation because they are associated with enhanced mixing, drag and dissipation (Farmer et al., 2002; Pawlak et al., 2003). All the processes usually observed around capes, like current separation, formation of eddies and generation of lee waves, result in a drag force imparted on the larger scale coastal flows. Obstacles can decelerate flows in two distinct ways: via tangential stresses over the surface of contact (skin drag), or via pressure differences across the obstacle (form drag). Recent studies associate the efficiency of the extraction of energy from coastal flows more with the obstacle shape than with the viscous dissipation due to bottom boundary layer processes. Moum and Nash (2000) and Nash and Moum (2001) find that, on a 5 km long obstacle, form drag exceeds skin friction by a factor of 2-3. According to the observations across Knight Inlet, Klymak and Gregg (2001, 2004) show that the form drag due to internal waves accounts for approximately 67% of the total energy dissipation and appears to be the major energy sink. It is followed by the drag due to horizontal eddies, bottom friction and internal dissipation. In the numerical simulations of Puget Sound and of the Strait of Juan de Fuca, both Lavelle et al. (1988) and Foreman et al. (1995) are obliged to use bottom drag coefficients about 5-10 times larger than the commonly used value (3×10^{-3}) in order to match observations. It is thought that the form drag associated with the unresolved topographic features present in the area is the cause of the missing dissipation (Edwards et al., 2004).

Since ocean coastlines are usually tortuous, and coastal areas are full of submerged topographic features like sills, straits and banks, the understanding of the processes influencing the form drag remains a critical point in modeling the ocean circulation realistically. This problem is inherently linked to the understanding of the conditions under which different coastal flow regimes appear. The theoretical study by MacCready and Pawlak (2001) shows that the form drag associated with a headland is affected by lee waves and eddy formation. However since they consider a small cape (~ 1 km) in a strongly stratified tidal system, their analysis neglects the Earth's rotation and their results cannot be applied to the cases with small Rossby numbers, namely for slower flows impinging on larger obstacles. Thus, it is not clear under which

42 conditions different flow regimes appear when rotation and stratification are
43 both important for the dynamics.

44 Coastal eddies are relevant to a range of coastal processes. Eddies behind capes
45 impact the distribution of marine organisms. They can constitute an effective
46 mechanism for larval retention (Chiswell and Roemmich, 1998; Roughan
47 et al., 2005), accumulation of juvenile clams (Rankin et al., 1994) and macro-
48 zooplankton assemblages (Murdoch, 1989). Coastal biologists are also inter-
49 ested in three-dimensional phenomena enhancing vertical mixing. For exam-
50 ple, there is evidence that strong upwelling around promontories can explain
51 a larger nutrient supply from the deeper layers and the subsequent increase in
52 primary production (John and Pond, 1992). Reproducing the characteristics
53 of these eddies is important also for effective coastal management. Since eddies
54 influence the pattern of sediment transport and deposition, they have to be
55 considered when sewage discharges or dredging activities are discussed (Pin-
56 gree, 1978; Bastos et al., 2002, 2003; Jones et al., 2006). For the same reason,
57 recirculations behind capes should be avoided when locations of offshore fish
58 cages are decided (Doglioli et al., 2004b).

59 Understanding the factors affecting eddy formation is challenging because the
60 dynamics of the processes involved are complex. Eddy generation is connected
61 to the phenomenon of current separation occurring in presence of obstacles
62 (Batchelor, 1967) and it can be explained in terms of adverse pressure gra-
63 dients and boundary layer detachment (Schlichting and Gersten, 2003). The
64 studies of homogeneous non-rotating flows usually consider a constant flow
65 impinging on a columnar (non-sloping) cylinder. They show the dependence
66 of the separation process on different non-dimensional parameters like the
67 Reynolds number, defined as $Re = UD/\nu$, where ν is the kinematic viscosity,
68 while U and D are the characteristic velocity and the horizontal dimension,
69 respectively (Batchelor, 1967). For $40 < Re < 1000$ a periodic eddy shedding
70 regime is established and, if f_s is the shedding frequency, the Strouhal number
71 $St = f_s D/U$ can be defined. In a homogeneous non-rotating flow, St is usu-
72 ally constant and equal to 0.21 (Kundu and Cohen, 2002). Even in complex
73 stratified and rotating conditions reproducing flows past islands, the Strouhal
74 number remains close to this value, being $St = 0.23$ (Dong et al., 2007). For
75 geophysical applications, Tomczak (1988) distinguishes between shallow and
76 deep water dynamics, depending on whether the dominant role of friction in
77 the system is played by lateral or vertical stresses. Following the same idea
78 and using the turbulent vertical viscosity ν_v^* , Wolanski et al. (1984) intro-
79 duce the so-called island wake parameter $P = (UH^2)/(\nu_v^* D)$. In analogy to
80 the Reynolds number, this parameter quantifies the importance of lateral ad-
81 vection relative to the vertical friction. Many studies show how P effectively
82 controls the flow around atolls and islands (Wolanski et al., 1996; Lloyd et al.,
83 2001; Stansby and Lloyd, 2001; Neill and Elliott, 2004). Since in shallow waters
84 bottom friction can be dominant, Pingree and Maddock (1980) use the bottom

85 drag coefficient C_D instead of ν_v^* . In this case, the importance of lateral advec-
86 tion relative to bottom friction is quantified by so-called equivalent Reynolds
87 number, $Re_f = H/(C_D D)$. If f is the Coriolis parameter, the Rossby number
88 $Ro = U/(fD)$ is also shown to control the eddy regime (Walker and Stew-
89 artson, 1972; Merkine and Solan, 1979; Boyer and Metz, 1983; Page, 1985),
90 while the β -effect inhibits the process of separation (Merkine, 1980; Boyer and
91 Davies, 1982). In a stratified, rotating fluid, the importance of stratification
92 in the separation process can be quantified in terms of the Burger number
93 $Bu = (R_d/D)^2$, where $R_d = NH/f$ is the baroclinic deformation radius, N is
94 the buoyancy frequency and H the characteristic vertical scale (Davies et al.,
95 1990b).

96 The theoretical results on flow separation in presence of obstacles are success-
97 fully used in many cases to explain the dynamics around islands (Heywood
98 et al., 1996; Tansley and Marshall, 2001; Coutis and Middleton, 2002). One
99 can be tempted to extend these results in a straightforward fashion also to the
100 case of capes. However, the dynamics of islands and capes can be significantly
101 different for at least two main reasons: the presence of a lateral coast and the
102 importance of sloping boundaries. Capes are not isolated features in the ocean
103 as atolls or volcanic islands, but they are connected with the mainland. The
104 presence of a coastline upstream and downstream the headland adds more lat-
105 eral friction to the system and reduces the degrees of freedom of fluid motion.
106 As a result, the critical Reynolds number needed to reach the eddy shedding
107 regime is higher than for cylinders (Verron et al., 1991) and flow separation
108 is somewhat inhibited. The Strouhal number decreases as a consequence and
109 in different conditions drops to the typical value of $St = 0.09$ (Boyer et al.,
110 1987; Davies et al., 1990a). Moreover, capes are usually embedded in the shelf
111 and in its slope, allowing for different processes to occur. Firstly, the pres-
112 ence of a sloping obstacle introduces potential vorticity constraints, reducing
113 barotropic instabilities and the tendency for eddy shedding (Klinger, 1993).
114 Secondly, flow separation and eddy formation are influenced by the shelf to-
115 pographic Rossby waves in a similar manner as the differential background
116 rotation (Freeland, 1990). Thirdly, in case of stratified waters, the presence of
117 a sloping obstacle allows the generation of lee waves (MacCready and Pawlak,
118 2001).

119 The study of cape dynamics relies on laboratory works (Boyer and Tao, 1987;
120 Boyer et al., 1987; Davies et al., 1990a), field experiments (Geyer, 1993; Farmer
121 et al., 2002; Pawlak et al., 2003; Edwards et al., 2004) and numerical results
122 (Verron et al., 1991; Signell and Geyer, 1991; Davies et al., 1995; MacCready
123 and Pawlak, 2001; Doglioli et al., 2004a).

124 The laboratory experiments of Boyer and Tao (1987) (hereinafter referred as
125 BT87) address the case of *rotating stratified* flows impinging on a triangular
126 prism cape with sloping sides. In the case of a right-side obstacle and for $Bu <$

127 0.2, the horizontal flow is fully-attached at all vertical levels. For somewhat
128 larger Burger numbers, $0.2 < Bu < 1$, an attached anticyclonic eddy slowly
129 forms in the lee of the obstacle. At still larger Burger numbers, $Bu > 1$, a
130 well-defined eddy shedding regime is established. The aspect ratio $\delta = H/D$
131 of laboratory experiments is generally very high compared to those in the real
132 ocean. As a result, the obstacle used in BT87 corresponds to a very steep cape
133 with slope $\alpha = 1$. As pointed out by the same authors, this geometry is far from
134 being realistic. Even in coastal environments where capes can be very steep,
135 the slope never reaches a value of $\alpha = 1$. Pawlak et al. (2003), for example,
136 report a cape with slope $\alpha = 0.2$; the promontory considered by Doglioli et al.
137 (2004a), instead, has $\alpha = 0.1$ while it is embedded in a much gentler sloping
138 shelf. The coastal headland studied by Geyer (1993) has a much lower slope,
139 $\alpha = 0.015$ and larger scale features like the Gargano Promontory reach much
140 lower values, like $\alpha = 0.004$ (Cushman-Roisin et al., 2007; Veneziani et al.,
141 2007). Therefore, it is not clear what is the role of topographic slope on the
142 flow regimes behind a cape and if the observations made by BT87 are still
143 valid for gentler slopes and more realistic scenarios.

144 The interplay between sloping capes, rotation and stratification leads also to
145 complicated three-dimensional dynamics. Near a coastal cape, Geyer (1993)
146 observes secondary circulations occurring in the vertical cross-stream plane.
147 He suggests that they are related to the presence of vertical shear in flows with
148 curvature (e.g. Kalkwijk and Booij, 1986). The same circulations can induce
149 significant upwelling (Alaee et al., 2004). Moreover, eddy tilting and internal
150 wave dynamics are proposed as mechanisms for the short eddy life-time ob-
151 served in tidal environments (Pawlak et al., 2003). Tilting and stretching of
152 coherent eddies are evident in presence of horizontal density fronts (Farmer
153 et al., 2002), where vertical velocities can reach extremely high values of up
154 to 0.5 m sec^{-1} , thereby suggesting a local increase in mixing.

155 However, most of the numerical studies focus on the case of shallow water
156 capes (Verron et al., 1991; Signell and Geyer, 1991; Davies et al., 1995), where
157 the flow can be considered homogeneous and obeying vertically-integrated
158 dynamics. Exceptions are the numerical works of Doglioli et al. (2004a) and
159 MacCready and Pawlak (2001) which are three-dimensional. However, the
160 former considers a winter non-stratified quasi-homogeneous flow, while the
161 latter neglects rotation. As a result, the effect of stratification in a rotating
162 environment for a relatively deep cape has not been extensively explored thus
163 far.

164 In this study, numerical simulations are carried out to pursue three main
165 objectives. The first objective is to assess the sensitivity of the generation
166 of turbulent coherent flow structures behind a cape to the combined effect
167 of stratification and rotation. We consider a geostrophically-balanced, steady
168 barotropic current impinging on a headland under different stratified condi-

169 tions. The second objective is to assess the effects of topographic slopes on the
170 flow regimes. In order to cover the large slope range found in the literature and
171 the ocean, we consider in our analysis five slopes: $\alpha = 1$, $\alpha = 0.1$, $\alpha = 0.02$,
172 $\alpha = 0.01$ and $\alpha = 0.005$. To our knowledge, this study represents the first
173 three-dimensional numerical and systematical effort assessing the changes in
174 the flow regimes at varying Burger numbers and slopes. The third objective is
175 to quantify the implications of the different regimes in the force drag imparted
176 from the cape to the coastal flow. In order to do that, we calculate the form
177 drag coefficients for all the cases so far considered.

178 In agreement with the laboratory experiments of [Boyer and Tao \(1987\)](#), we
179 find that the separation process is enhanced for increasing Bu . However, when
180 gentler slopes similar to oceanic ones are considered, the importance of bot-
181 tom friction increases and the same process is gradually more inhibited. Flow
182 regimes diagrams in the $Bu - \alpha$ space show that bottom friction is important
183 especially near the bottom when $Bu \geq 1$. We also find that the form drag co-
184 efficient is at least 100 fold greater than the skin drag one and it reaches larger
185 values for increasing Burger numbers and decreasing slopes. We empirically fit
186 the values obtained from the runs to express with a function the dependency
187 of the form drag coefficient on Bu and α .

188 The paper is organized as follows. In section 2 the numerical model is presented
189 together with a description of the numerical setups for all the simulations.
190 The results are presented in section 3. In particular, sections 3.1 and 3.2 show
191 the appearance of different flow regimes when the Burger number and the
192 topographic slope are varied. Section 3.3 discusses the implication of these
193 regimes on the different drags imparted on the coastal flow. A summary and
194 concluding remarks are given in section 4.

195 2 Method

196 2.1 Numerical model

197 The numerical model used in this study is the Regional Ocean Modeling Sys-
198 tem (ROMS). ROMS solves the primitive equations and it is a hydrostatic
199 terrain-following (sigma) coordinate model ([Shchepetkin and McWilliams,](#)
200 [2005](#)). Sigma coordinates are particularly useful in coastal applications be-
201 cause they resolve bottom boundary layer processes.

202 Since geophysical flows are characterized by large Reynolds numbers, in this
203 study we decide to use ROMS ability to run with zero explicit numerical viscos-
204 ity ν^* and to just use the implicit viscosity built into the third-order, upstream-

CONSTANT PARAMETERS					
<i>Dimensional</i>			<i>Non-dimensional</i>		
H [m]	S_{bot}	Temp. [$^{\circ}$ C]	C_D	Ro	Re^*
81	35	12.5	3×10^{-3}	0.06	Implicit

Table 1
Constant parameters for all the simulations.

205 biased advection operator (Shchepetkin and McWilliams, 1998). The effective
206 turbulent Reynolds number $Re^* = UD/\nu^*$ is then established by the resolution
207 of the grid: it represents the largest affordable Re^* with a certain discretiza-
208 tion. The simulations are run with the ROMS default generic length scale
209 algorithm (Umlauf and Burchard, 2003) which defines a $k - \epsilon$ turbulence clo-
210 sure with Canuto-A stability functions (Canuto et al., 2001). The skin bottom
211 friction stress is calculated directly by the model according to the quadratic re-
212 lation $\vec{\tau}_b = -\rho_0 C_D \vec{v}_b \sqrt{u_b^2 + v_b^2}$, where $\vec{v}_b \equiv (u_b, v_b)$ is the bottom velocity and
213 ρ_0 the water density. The skin drag coefficient is set to $C_D = 3 \times 10^{-3}$. No-slip
214 boundary conditions are simulated by the model via a specific land-masking
215 rule (see discussion in Dong et al., 2007) even when $\nu^* = 0$ (Shchepetkin and
216 O’Brien, 1996).

217 2.2 Numerical setup

218 Coastal capes have characteristic horizontal dimensions which can scale from
219 $D \sim 1$ km to $D \sim 100$ km. In the case of shallow waters ($H \sim 10$ m), the
220 dynamics around headlands are known to be dominated by bottom frictional
221 effects (Signell and Geyer, 1991; Davies et al., 1995). For relatively deep waters
222 ($H \sim 100$ m) the dynamics are less clear and more interesting. Complicated
223 three-dimensional phenomena are shown to take place and to be strongly
224 dependent on the system parameters (Geyer, 1993; Farmer et al., 2002; Pawlak
225 et al., 2003; Doglioli et al., 2004a). In these cases, if typical values of $C_D \sim$
226 10^{-3} , $f \sim 10^{-4} \text{ sec}^{-1}$, $U \sim 0.1 \text{ m sec}^{-1}$ and $N \sim 3 \times 10^{-3} \text{ sec}^{-1}$ are considered,
227 it is possible to calculate realistic ranges for the parameters Ro , Bu and Re_f ,
228 namely: $10^{-2} < Ro < 1$; $10^{-3} < Bu < 10$; and $1 < Re_f < 100$.

229 In all the simulations the obstacle is a triangular prism with sloping bound-
230 aries lying on a flat bottom (see Fig. 1b) and the domain of integration is a
231 zonal channel discretized with a rectangular unevenly spaced grid of $285 \times$

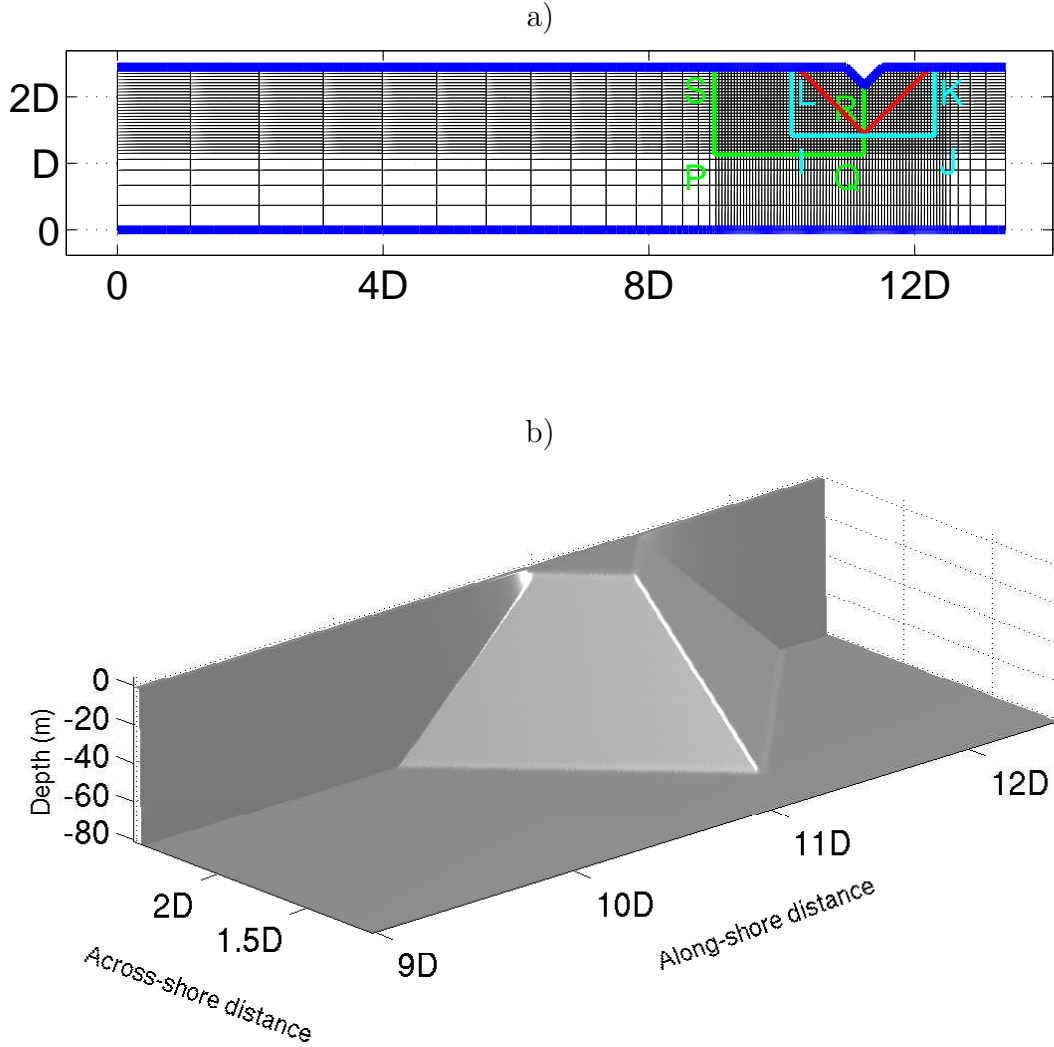


Fig. 1. Numerical setup expressed in terms of D . D is defined as the across-shore horizontal dimension of the obstacle at the bottom. a) Plan view of the horizontal grid. For clarity, every third grid-point is shown in the picture. The northern and southern boundaries are closed (blue thick line) while the eastern and western are open. The red line indicates where the slope terminates. The areas IJKL (cyan) and PQRS (green) are functional to later calculations of the kinetic energy and the form drag, respectively. b) Three-dimensional shape of the cape.

232 100 points (Fig. 1a). The mesh size increases in both the along and across
 233 directions moving away from the obstacle. The most resolved interior area
 234 around the cape has a horizontal resolution of $\Delta = D/65$ in all the simula-
 235 tions, while the vertical resolution relies on 20 sigma layers. Open boundaries
 236 are located at the east and at the west of the domain while a no-slip condition
 237 on a rigid wall is implemented at the north and at the south (see Fig. 1a). The
 238 simulations are forced by inflow conditions at the open boundaries. Here the

		<i>Bu</i>								
		0.0	0.05	0.10	0.30	0.50	0.70	1.00	3.00	6.48
Slope (α)	1	x	x	x	x	x	x	x	x	x
	0.1		x					x		x
	0.02		x					x		x
	0.01		x	x	x	x		x		x
	0.005		x			x		x		

Table 2
The matrix of the numerical simulations for this study.

239 Flather condition is used for the averaged velocities, while radiation conditions
 240 are used for the sea surface height, baroclinic velocities and the tracers. At
 241 the boundaries the tracers are relaxed toward the initial values in an area of
 242 six grid points to facilitate the radiation outside the numerical domain. The
 243 stratification is induced by a linear increase in the initial salt distribution with
 244 depth, while the temperature is held constant.

245 In all simulations, the characteristic vertical dimension is set to $H = 81$ m,
 246 the constant temperature to 12.5°C and the bottom salinity to $S_{bot} = 35$ (the
 247 surface value S_{surf} is varied at varying stratification). The Rossby number Ro
 248 is also held fixed at the realistic value of $Ro = 0.06$, that is very close to
 249 the one used in the photographed experiments of BT87 thus allowing for a
 250 convenient visual comparison between our results and the ones observed in
 251 the laboratory. The parameters held always constant are listed in Table 1.

252 The main non-dimensional parameters varied in this study are the Burger
 253 number Bu and the slope of the obstacle α . We span the ranges $0 \leq Bu \leq 6.48$
 254 and $0.005 \leq \alpha \leq 1$ (Table 2). The horizontal dimension D , the rate of rotation
 255 f , the surface salinity value S_{surf} and the inflow unperturbed velocity U are
 256 varied according to the values of Bu and α , with the additional constraint of
 257 constant Ro . The whole set of dimensional and non-dimensional values for the
 258 performed experiments are listed in Table 3. The first block of nine experi-
 259 ments cover the range of the BT87 laboratory experiments, characterized by
 260 $\alpha = 1$ and increasing Bu . The other experiments investigate the dynamics at
 261 gentler (and more realistic) slopes.

262 The external value for the normal velocity to the open boundaries is prescribed
 263 according to the Rossby number $U_b = Ro f D$, while the value for the sea
 264 elevation is needed to sustain geostrophically with its gradient such a veloci-

VARIABLE PARAMETERS						
	<i>Dimensional</i>				<i>Non-dimensional</i>	
Exp.	D [km]	U [m sec ⁻¹]	f [sec ⁻¹]	S_{srf}	Slope (α)	Bu
1	0.13	0.078	10 ⁻²	35.00	1	0.00
2	0.13	0.078	10 ⁻²	34.86	1	0.05
3	0.13	0.078	10 ⁻²	34.74	1	0.10
4	0.13	0.078	10 ⁻²	34.18	1	0.30
5	0.13	0.078	10 ⁻²	33.64	1	0.50
6	0.13	0.078	10 ⁻²	33.08	1	0.70
7	0.13	0.078	10 ⁻²	32.27	1	1.00
8	0.13	0.078	10 ⁻²	26.76	1	3.00
9	0.13	0.078	10 ⁻²	17.61	1	6.48
10	1.30	0.078	10 ⁻³	34.86	0.1	0.05
11	1.30	0.078	10 ⁻³	32.27	0.1	1.00
12	1.30	0.078	10 ⁻³	17.61	0.1	6.48
13	6.50	0.039	10 ⁻⁴	34.96	0.02	0.05
14	6.50	0.039	10 ⁻⁴	34.32	0.02	1.00
15	6.50	0.039	10 ⁻⁴	30.52	0.02	6.48
16	13.0	0.078	10 ⁻⁴	34.86	0.01	0.05
17	13.0	0.078	10 ⁻⁴	34.74	0.01	0.10
18	13.0	0.078	10 ⁻⁴	34.18	0.01	0.30
19	13.0	0.078	10 ⁻⁴	33.64	0.01	0.50
20	13.0	0.078	10 ⁻⁴	32.27	0.01	1.00
21	13.0	0.078	10 ⁻⁴	17.61	0.01	6.48
22	26.0	0.156	10 ⁻⁴	34.45	0.005	0.05
23	26.0	0.156	10 ⁻⁴	29.52	0.005	0.50
24	26.0	0.156	10 ⁻⁴	24.00	0.005	1.00

Table 3
Varying parameters for all the simulations.

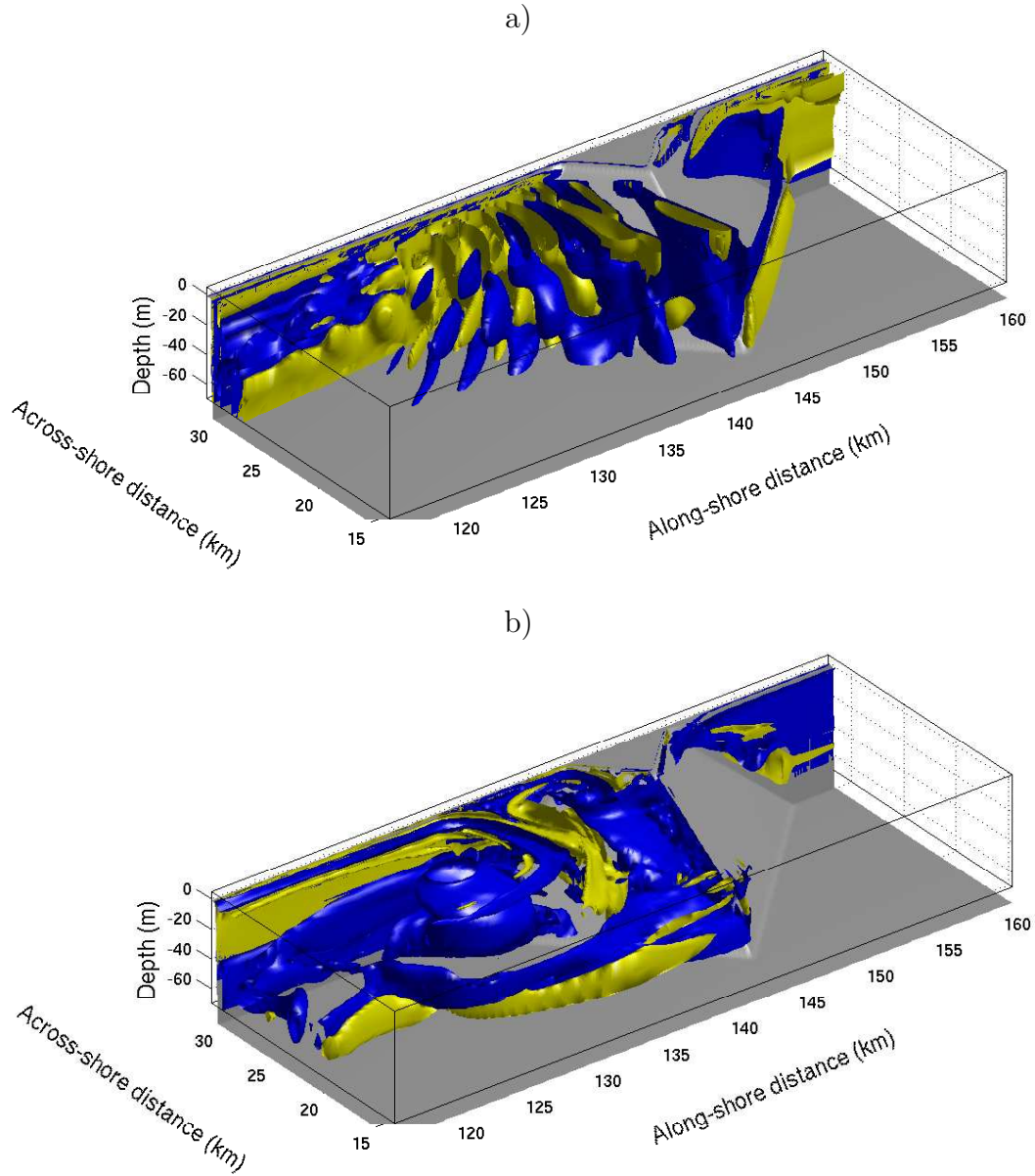


Fig. 2. Three-dimensional views of relative vorticity iso-surfaces in the vicinity of the cape. Negative values are shown in blue, while positive values are in yellow. a) Exp. 16: a typical example of fully-attached regime, when no separation occurs and lee waves are evident in the lee of the obstacle. b) Exp. 21: an example of eddy shedding regime. The flow is almost two-dimensional and flow separation is observed behind the cape.

265 ty. The value for the tangential velocity is set to $V_b = 0$ m/s. To simulate a
 266 sudden start comparable with the BT87 experiment, all the simulations begin
 267 with $U = U_b$ prescribed in the whole domain.

268 The simulations run until $\tau = 25.92$, where τ is the dimensionless advective
269 time defined as $\tau = tU/D$. Time-steps are varied always respecting the CFL
270 condition. For example, the nine simulations for the first set of experiments are
271 run with baroclinic and barotropic timesteps of $\Delta t_i = 0.5$ sec and $\Delta t_e = 0.025$
272 sec, respectively. In order to achieve $\tau = 25.92$, the model cycles in this case
273 for 86400 time iterations and each simulation requires a wall-clock time of four
274 days using a single processor.

275 For the same typical values, the β -effect is expected not to play a significant
276 role, since $10^{-4} < \beta D/f < 10^{-2}$. In contrast, topographic Rossby effects can
277 be relevant, given the steep slope of some cases. However, this study is limited
278 to the case where the obstacle lies on the right hand side of the in-coming
279 current and we expect topographic waves not to alter the flow significantly
280 because they propagate in the same direction as the main current (Freeland,
281 1990).

282 3 Results

283 Different flow regimes can be observed in the numerical experiments listed
284 in Table 3. Fig. 2 provides a visual idea of flow regimes at constant slope
285 ($\alpha = 0.01$) but at different Burger numbers. It also underlines the complexity
286 and the three-dimensional structure of the different turbulent features appear-
287 ing behind the cape. Fig. 2a shows vorticity surfaces for the fully-attached
288 regime when $Bu = 0.05$. In this case the horizontal flow follows the obstacle
289 at different vertical levels and no separation behind the obstacle is observed.
290 Vertical movements are due to the presence of lee waves evident as elongated
291 oscillating structures behind the obstacle. Fig. 2b shows an eddy shedding
292 regime when $Bu = 6.48$. Vertical movements are restricted and the flow is
293 more two-dimensional. As a result, a separation area is observed behind the
294 obstacle and coherent eddies form behind the cape.

295 To put order in describing the totality of the regimes, it is convenient to
296 initially restrict our attention to simulations having the same parameters of
297 the BT87 laboratory experiments. We then consider gentler slope cases as the
298 ones that can be found in the ocean.

299 3.1 Flow regimes for $\alpha = 1$

300 We first analyze the case with $\alpha = 1$ to compare the flow regimes obtained
301 running ROMS with the BT87 laboratory experiment. It is useful to recall
302 the main findings of the BT87 work. For a right side obstacle, BT87 show the

303 appearance of three different regimes corresponding to a gradual increase of
304 stratification: (i) a fully-attached regime for low Burger numbers ($Bu < 0.2$),
305 (ii) an eddy-attached regime for intermediate Burger numbers ($0.2 < Bu < 1$)
306 and (iii) an eddy shedding regime for high Burger numbers ($Bu > 1$).

307 Figures 3 and 4 show vorticity and velocity snapshots obtained when the nu-
308 merical model is integrated. The fields are shown at three different depths and
309 for increasing Bu . In the homogeneous case ($Bu = 0.00$, Fig. 3a, b and c), po-
310 tential vorticity conservation constrains the generation of small anticyclones in
311 the stripe over slope topography. However, since the geometry of the obstacle
312 is symmetric, an upstream decrease in relative vorticity due to the presence of
313 shallower waters corresponds with an equal downstream increase as the waters
314 become deeper. As a result, all the vorticity gradients are confined above the
315 slope and nothing significant can be observed downstream the obstacle at any
316 depth.

317 The presence of stratification, even if very weak, changes the dynamics. For
318 small Burger numbers, $Bu = 0.05$, no eddies are present. The flow tends to
319 follow the obstacle at all levels (fully-attached regime, Fig. 3d, e and f). At
320 the same time, a clear oscillating signal in the vorticity field can be observed
321 starting from the tip of the cape and continuing downstream. The signal is
322 associated with the formation of lee waves as the flow goes over the ridge of
323 the cape. If we increase further the Burger number, $0.10 \leq Bu \leq 0.30$, small-
324 scale eddies form at surface in the lee of the cape and they drift downstream
325 away from the obstacle as isolated small features (Fig. 3g). The strongest
326 of these smaller eddies come from the area close to the tip of the cape. We
327 therefore refer to this turbulent regime as tip-eddy regime. At depth some
328 of these tip eddies merge to form larger scale structures (Fig. 3h and i). For
329 higher Burger numbers, $0.50 \leq Bu \leq 0.70$, the same structures gradually grow
330 and occupy all the space available in the lee of the cape. Their diameter is
331 comparable at every depth with the across-shore obstacle dimension at that
332 level. We refer to these larger eddies as lee eddies. Due to the direction of
333 the incoming current, the first eddy forming in the lee is an anticyclone. Its
334 interaction with the sides of the obstacle causes the formation of a lee cyclone.
335 This latter also grows in time and, with its growth, it allows the detachment
336 of the first eddy from the wall. At the same time a second lee anticyclone
337 can start forming. When the second lee anticyclone occupies the whole lee of
338 the cape, the cyclone is also pushed downstream and it sheds from the cape.
339 The cyclone interacts with the first anticyclone forming an eddy pair which
340 advects downstream. Once the pair sheds from the cape, a second one forms
341 in the lee and the cycle is repeated. For these Bu values, an eddy shedding
342 regime is therefore established. Initially the lee eddies are weak and they do
343 not appear as coherent vorticity features even if their strength increases with
344 depth (Fig. 4a, b and c). A weaker signal of the presence of lee waves can still
345 be observed at surface, while at the bottom, smaller tip eddies still form close

$$\alpha = 1$$

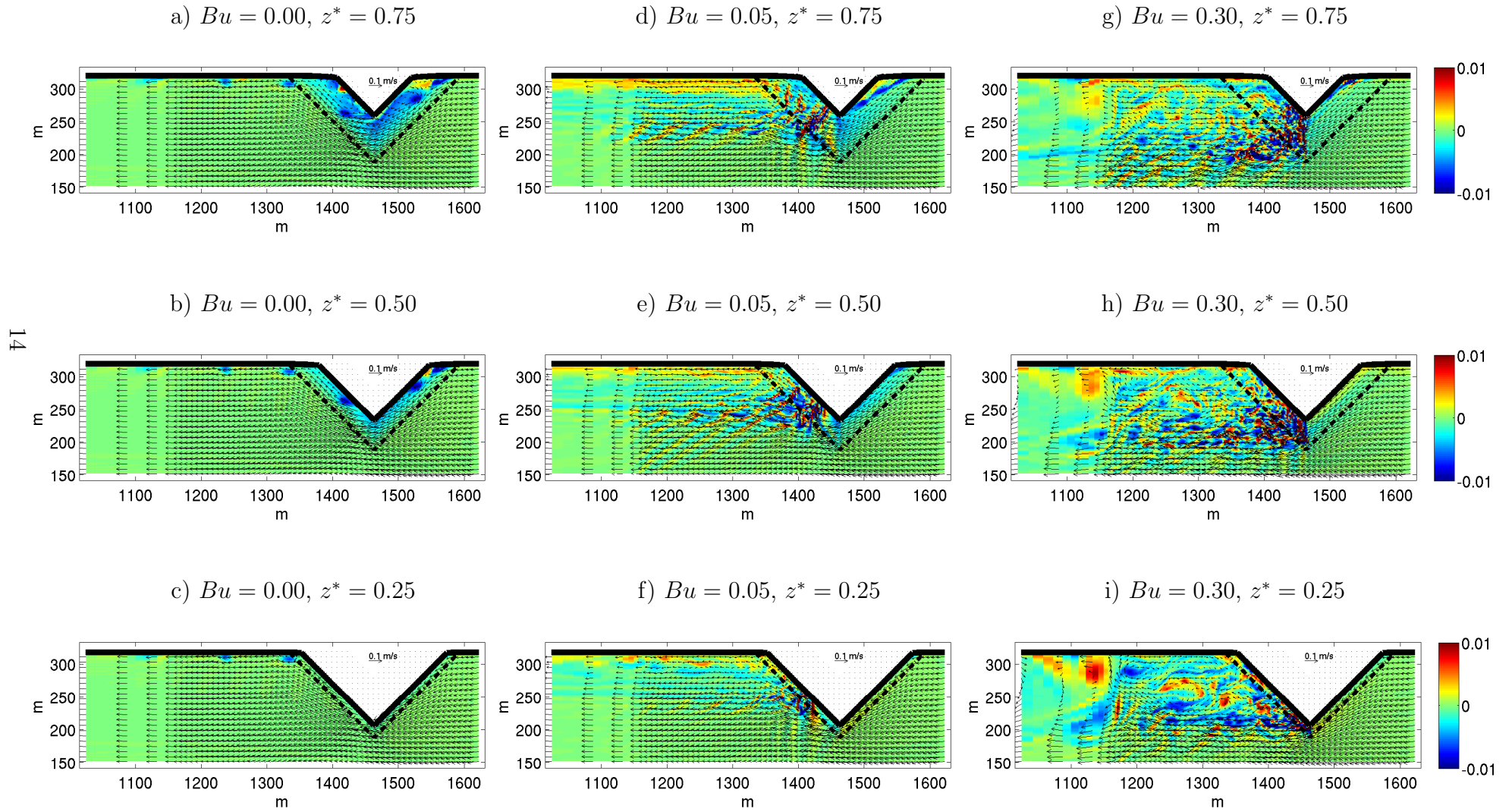


Fig. 3. Close up of relative vorticity [sec^{-1}] and velocity vectors at three different levels of the water column ($z^* = z/H$) after $\tau = 9.936$ for the $\alpha = 1$ simulations. The black dash-dotted line indicates where the slope terminates.

$$\alpha = 1$$

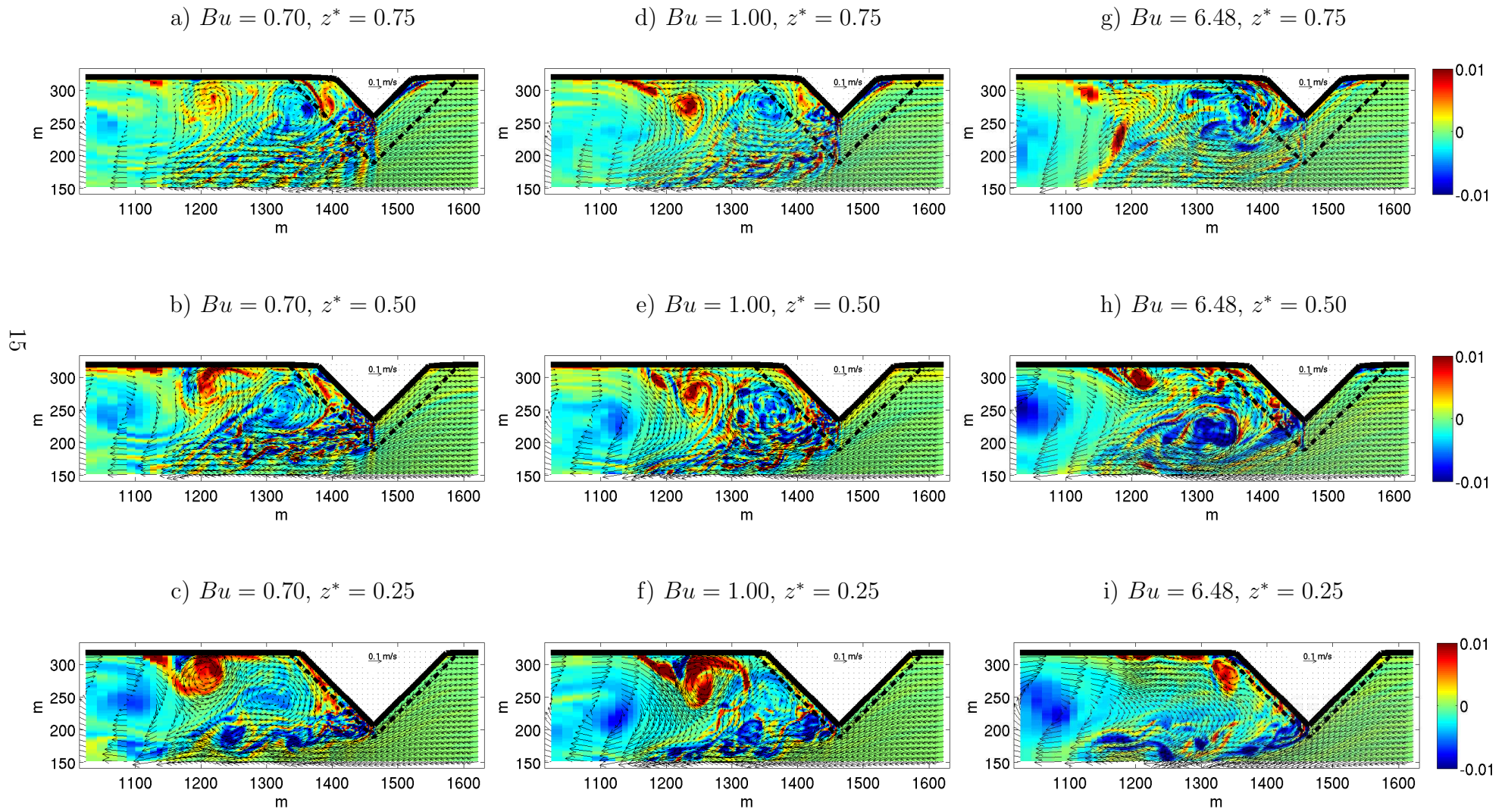


Fig. 4. As in Fig. 3 but for different Bu .

346 to the apex of the obstacle and they are advected along the periphery of
 347 the larger lee anticyclone. For $Bu = 1.00$, the eddy shedding regime is more
 348 evident because the eddies are stronger and more coherent than before at all
 349 depths (Fig. 4d, e and f). Finally, for large stratification, $Bu = 6.48$, the eddies
 350 are more elongated and stronger (4g, h and i).

351 In our simulations, two of the regimes observed in the laboratory are evident.
 352 For $Bu < 0.1$ the fully-attached regime appears behind the obstacle as well
 353 as the eddy shedding for $Bu \geq 1$ values. For intermediate Bu , however, the
 354 numerical model makes a rapid transition from the fully-attached regime to
 355 tip eddies which gradually organize and shed more for increasing stratifica-
 356 tions. Irrespective of the value for Bu , the BT87 eddy-attached case is not
 357 reproduced in our runs and seems to describe only a transitional state be-
 358 tween the fully-attached and the eddy shedding regimes. We speculate that
 359 its relative importance in the laboratory experiments should be attributed
 360 to important features which cannot be reproduced in our simulations. For
 361 example, the BT87 experimental apparatus has a rigid Plexiglas lid on the
 362 top of the tank. This lid can introduce additional friction and the same au-
 363 thors observe spin down effects on the weaker turbulent structures at the
 364 surface of the tank. Moreover, at the high aspect ratio of the BT87 case, the
 365 hydrostatic approximation can be questionable even if, for small Rossby num-
 366 bers, the dynamics should remain hydrostatic. Pedlosky (1987) shows that the
 367 hydrostatic limit occurs when $l_{hydr} = \min(\delta^2, \delta^2 Ro) \ll 1$, and in this study
 368 $1.5 \times 10^{-6} < l_{hydr} < 6 \times 10^{-2}$. Finally it is important to underline the difference
 369 between Reynolds numbers used in laboratory experiments versus numerical
 370 simulations. BT87 deal with a real fluid, characterized by its viscosity and
 371 Reynolds number Re . Ocean models, instead, have to rely on numerical vis-
 372 cosity ν^* to remove and avoid accumulation of energy at smaller scales. Our
 373 simulations run with the different turbulent Reynolds number Re^* .

374 The normalized kinetic energy budget, KE/KE_0 , calculated over the area
 375 PQRS of Fig. 1, is used to follow the temporal evolution of the flow. Here
 376 $KE_0 = KE(z, t = 0)$. KE/KE_0 is shown at the surface and near the bottom
 377 for varying Bu in Fig. 5. When $Bu = 0.05$, where no separation occurs,
 378 KE/KE_0 remains flat and steady at all levels and times. When $Bu = 0.30$,
 379 an oscillating signal appears. This is consistent with the emergence of the tip
 380 eddies regime observed before. When $Bu = 0.50$, the lee eddy shedding regime
 381 is evident in the kinetic energy pattern. We can easily count four distinct
 382 maxima. The shedding regimes appear to be in phase at different levels and
 383 stronger with increasing depths. For increasing Bu , the shedding regimes are
 384 always in phase and gradually more energetic. However, the number of peaks
 385 associated with the shedding decreases.

386 Summarizing, in the $\alpha = 1$ case, we can observe a clear general trend for
 387 varying Burger numbers. For low Bu we observe a fully-attached regime while,

$$\alpha = 1$$

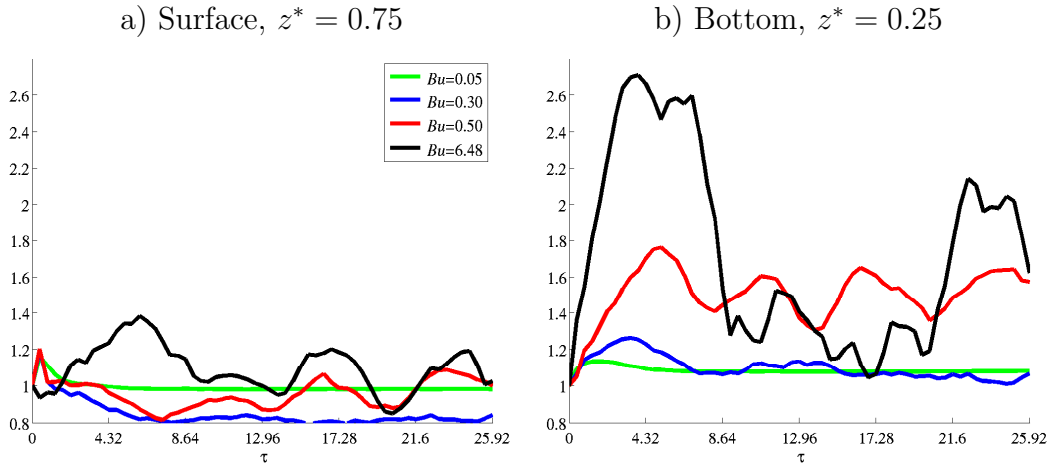


Fig. 5. The ratio KE/KE_0 in time for varying Burger numbers Bu . The obstacle slope is $\alpha = 1$ in all the considered simulations.

388 increasing the Burger number, eddy generation is gradually more evident until
 389 a clear shedding regime is established for higher Bu . These results match well
 390 the idea that the eddy shedding regime is enhanced if the flow remains more
 391 horizontal than vertical. If stratification is increased, vertical movements are
 392 also reduced and fluid particles are forced to go more around the obstacle than
 393 over it. As a result their trajectories are more and more two-dimensional and
 394 the separation process is more probable to appear than lee wave generation.

395 3.2 Flow regimes for $\alpha < 1$

396 We now describe the results when different obstacle slopes are considered for
 397 varying Burger numbers. With respect to the previous $\alpha = 1$ case, bottom
 398 friction is expected to be more influential for gentler slope simulations. In an-
 399 analyzing our results, we have to take into account contrasting effects. On one
 400 hand, bottom friction is expected to gradually damp turbulent structures with
 401 gentler slopes, inhibiting lee eddy formation. On the other hand, high stratifi-
 402 cation values are expected to gradually favor separation and eddy generation
 403 in the surface layers for two different reasons. Firstly, strong stratification re-
 404 duces vertical movements forcing particle trajectories to be more and more
 405 two-dimensional. Secondly, a strong stratification shields surface layers from
 406 bottom friction confining its inhibiting effect more to the deeper layers.

407 These effects can be clearly seen in the $\alpha = 0.01$ cases (Fig. 6). For $Bu = 0.05$,
 408 the regime is again fully-attached even if the lee wave signal is less noisy. Its
 409 intensity decreases with depth and lee waves almost disappear in the layer
 410 closer to the bottom (Fig. 6a, b and c). When $Bu = 1.00$, bottom friction
 411 influences most of the water column since stratification is still not so important
 412 to shield the top layers. Near the surface an eddy shedding can still be observed
 413 and the sequence of eddy pairs is very regular and periodic (Fig. 6d). In
 414 the middle of the water column, the evident eddy shedding regime of the
 415 steeper case is generally inhibited. Moreover, after the formation of the first
 416 lee anticyclone, different tip eddies move along its periphery while the lee
 417 eddy does not shed and stays attached to the cape. The occasional presence
 418 of small cyclones allows the shedding of small features from the tail of the
 419 lee anticyclone. As a result, the detachment of the eddies from the cape does
 420 not happen at the lee but further downstream (Fig. 6e). At the bottom, the
 421 anticyclone rapidly decays due to bottom friction and the eddy shedding is
 422 just due to tip eddies traveling around its periphery (Fig. 6f). For $Bu = 6.48$,
 423 the increasing stratification limits frictional effects to near bottom layers. At
 424 the surface and in the middle of the water column, stronger and wider lee
 425 eddies form downstream the cape. They become more elongated to finally
 426 detach much later from the obstacle than for $Bu = 1.00$ (Fig. 6g and h). At
 427 the bottom, the initial strong lee anticyclone spins down and the tip eddy
 428 shedding almost completely disappears. What is left is a big separation area
 429 which remains attached to the cape for the rest of the simulation (Fig. 6i).
 430 We refer to this situation as an eddy-attached regime.

431 Summarizing in the $\alpha < 1$ case, namely for slopes similar to the oceanic ones,
 432 bottom frictional effects are more important than in the laboratory experi-
 433 ments. For gentler cases, lee eddies are larger and bottom friction can act on
 434 the wider bottom eddy surface. As a result, bottom friction damps and spins
 435 down turbulent structures and bottom flow regimes can differ from surface
 436 ones.

437 As before, we can visualize the time trends of the flow regimes with the help
 438 of the ratio KE/KE_0 . In order to assess just the role of the obstacle slope,
 439 here we just choose to show the simulations with $Bu = 1.00$ and where just
 440 α is varied. Fig. 7 shows the values for KE/KE_0 at the surface and at the
 441 bottom. When $\alpha = 1$, an eddy shedding regime is present. The maxima due
 442 to the shedding are three and in phase at different depths. They are more
 443 energetic if we move toward the bottom layers. For $\alpha = 0.1$, the effect of
 444 bottom friction starts to be felt. At all depths the shedding is less energetic
 445 than before. However the frequency of the peaks slightly increases even if the
 446 layers are still in phase with each other. A drastic difference is observed for
 447 gentler slopes. For $\alpha = 0.05$, the shedding regime is so reduced that the flow
 448 can be considered eddy-attached while, at the surface, three distinct peaks
 449 can still be found. For gentler slopes, $\alpha = 0.01$ and $\alpha = 0.005$, these trends

$$Bu = 1.00$$

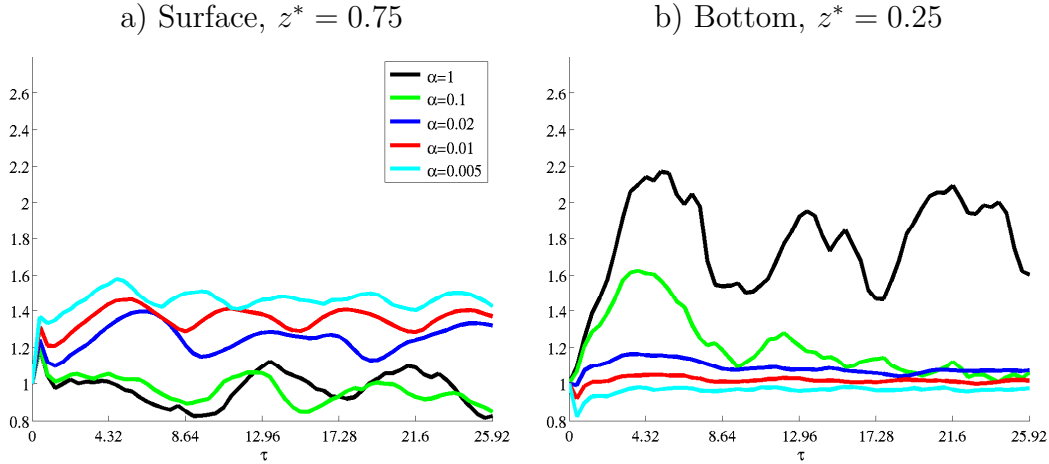


Fig. 7. The ratio KE/KE_0 in time for varying obstacle slopes α . The Burger number is $Bu = 1.00$ in all the considered simulations.

450 are gradually more evident. At the bottom the first lee eddy does not form
 451 and just tip eddies can be observed. At surface, the lee eddy shedding still
 452 persists and the shedding frequency gradually increases for gentler slopes. We
 453 can count four maxima for $\alpha = 0.01$ and five when $\alpha = 0.005$.

454 Since KE/KE_0 accurately reflects the flow characteristics shown in the snap-
 455 shots, we can use the time evolution of this quantity to tell apart the different
 456 flow regimes in the simulations. The concept behind this idea is the follow-
 457 ing. In the case of a fully-attached regime, the KE/KE_0 trend is completely
 458 flat and steady in time and this is reflected in a very low standard deviation.
 459 The emergence of tip eddies increases the time variability of the trend and
 460 the standard deviation is expected to slightly increase. When a lee eddy shed-
 461 ding regime appears, the variability increases more while, for a more energetic
 462 lee eddy shedding regime, it is expected to result even larger. The only flow
 463 regimes escaping this simple criterion are the ones strongly influenced by bot-
 464 tom friction. In this cases, the effect of the bottom is so important as to spin
 465 down the first lee eddies. If the eddy shedding is initially very energetic, bot-
 466 tom friction gradually weakens the flow and the intensity of the eddies shed.
 467 Otherwise, bottom friction spins down the first lee anticyclone so much to
 468 establish an eddy-attached regime. Both these cases, however, are easily rec-
 469 ognizable since KE/KE_0 neither stays flat nor oscillates. Rather, it decays in
 470 time indicating a gradually weakening of the flow. Details of this classification
 471 are reported in the appendix.

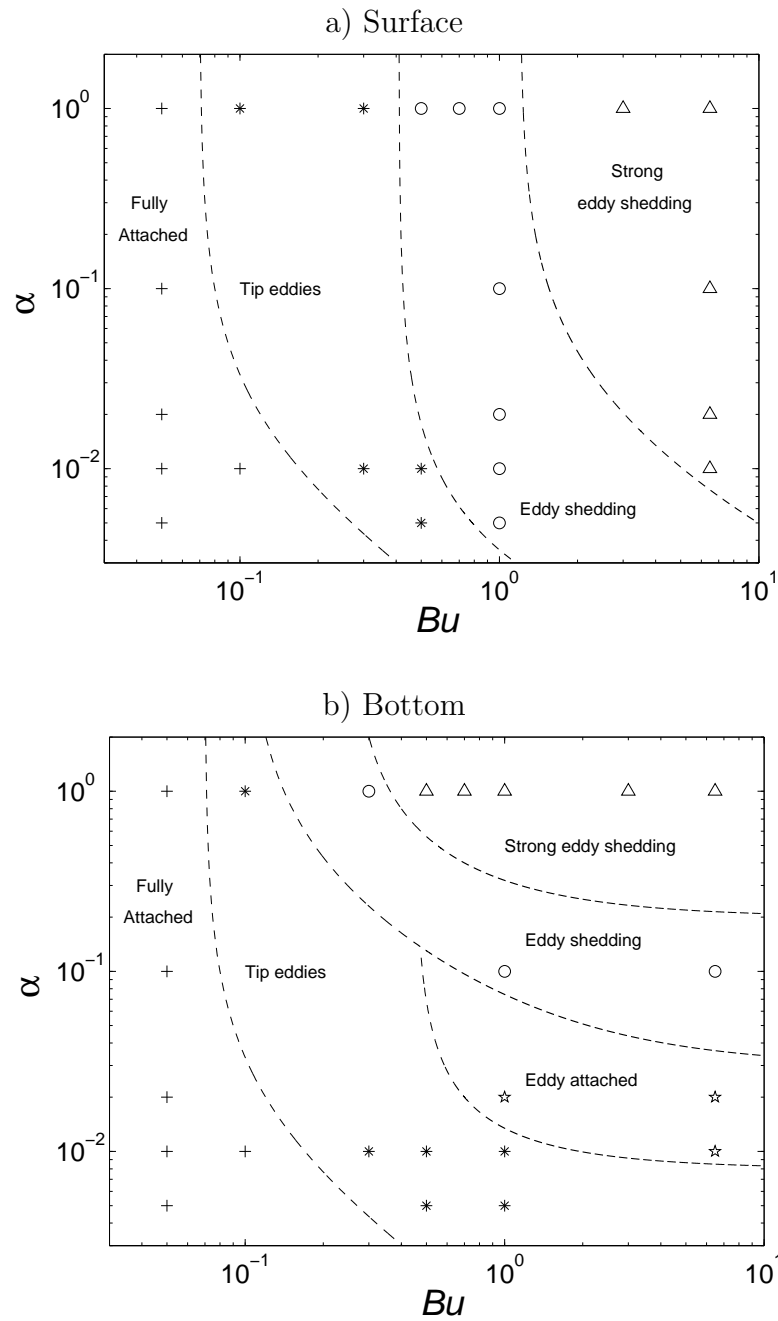


Fig. 8. Different regimes varying Bu and the slope α for a) surface and b) bottom. Note that both axes are logarithmic. The regimes are: fully-attached (+), tip eddies (*), eddy-attached (\star), eddy shedding (o) and strong eddy shedding (Δ). The dashed lines are the approximate divisions between the regimes.

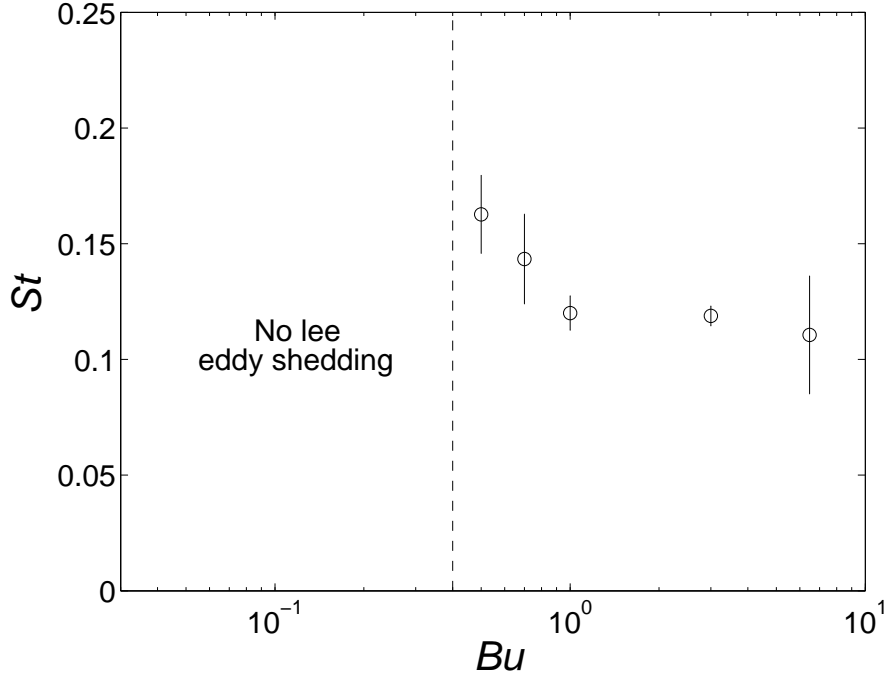


Fig. 9. Strouhal number as a function of Bu for $\alpha = 1$. Error bars indicate standard deviations.

472 Once this classification is performed, a flow regime diagram in the $Bu - \alpha$
473 space can be drawn. Figures 8a and 8b show this diagram for the surface
474 and the bottom layer, respectively. Figure 8a underlines how surface regime
475 are strongly dependent on Bu and almost independent of α . For low Bu , the
476 fully-attached regime extends for all the slope values considered in this study.
477 For high aspect ratios and increasing Bu , tip eddies are followed by a lee eddy
478 shedding regime. For high Bu this regime becomes stronger and more evident.
479 When we decrease the slopes, a general inhibition due to bottom friction effects
480 can be observed. The eddy shedding regime is gradually reached at higher Bu
481 and, for most of the intermediate Burger numbers, it is replaced by tip eddies.
482 This shift in the regime happens more gradually for gentler slopes.

483 The situation changes for the layer close to the bottom since for $Bu \geq 1$
484 the dynamics are controlled by α . When $\alpha = 1$, the scenarios are similar to
485 the surface. This is expected since the bottom friction does not play such a
486 role for high aspect ratios. For gentler cases, lee eddies are larger and their
487 surface in contact with the sea-floor is proportionally wider. Bottom friction
488 can decelerate the flow and spin down the first lee eddy forming. As a result,
489 the strong eddy shedding gradually disappears and eventually leaves space to
490 the eddy-attached regime. When the importance of bottom friction increases
491 more, a lee eddy cannot even form and we are left just with small tip eddies.

492 The time evolution of KE/KE_0 of Fig. 5 and 7 already shows important differ-
 493 ences in the lee shedding frequency. In order to quantify these differences, the
 494 Strouhal number is calculated. The period of the shedding is measured by the
 495 time taken for the centers of successive anticyclones to pass the across-shore
 496 section \overline{PQ} shown in Fig. 1a. Fig. 9 indicates that St decreases for increasing
 497 Burger numbers and for high Bu gets close to the value 0.09 registered in other
 498 works under different conditions (Boyer et al., 1987; Davies et al., 1990a).

499 3.3 Form drag

500 The drag associated to pressure differences across an obstacle can be much
 501 larger than the frictional drag and represent the dominant mechanism to decel-
 502 erate the coastal flow impinging on an obstacle (Moum and Nash, 2000; Mac-
 503 Cready and Pawlak, 2001; Edwards et al., 2004; Klymak and Gregg, 2004).
 504 Changes in the momentum can result from skin friction as well as from the
 505 form drag associated to these differences (Baines, 1995; Kundu and Cohen,
 506 2002). In this section of the paper, we want to quantify and compare form and
 507 frictional drags and to assess which physical processes are the cause for their
 508 different values in the various simulations.

509 If the sea surface height and the bottom surface are respectively at $z =$
 510 $\eta(x, y, t)$ and at $z = b(x, y)$, ρ the density field, ρ_0 a constant background
 511 density, $\rho' = \rho - \rho_0$, and g the gravitational acceleration, the internal pressure
 512 associated with the deformation of the isopycnals upstream and downstream
 513 the cape can be calculated as $p_{int}(x, y, t) = \int_b^\eta g\rho' dz$ (McCabe et al., 2006). We
 514 can then assume the pressure to be hydrostatic and split the contribution due
 515 to the sea surface elevation from the one due to p_{int} . Following the literature,
 516 these two different contributions are referred as external and internal form
 517 drags, respectively.

518 We normalize the drag forces for the different simulations using the charac-
 519 teristic velocity U , the density ρ_0 and a suitable area. For the form drags, the
 520 projected frontal area of the obstacle A_{front}^{proj} is used, while, for the effective skin
 521 bottom drag, we use the surface of contact A_{cont} on which the bottom stress
 522 can act. This non-dimensionalization allows a comparison of the results in
 523 terms of the magnitude of the commonly used drag coefficient. The following

524 expressions are therefore used:

$$525 \quad C_{D \text{ Fric}}^{Eff}(t) = \frac{1}{\rho_0 U^2 A_{cont}} \int_{y_1}^{y_2} \int_{x_1}^{x_2} \tau_b^x(x, y, t) dx dy, \quad (1a)$$

$$526 \quad C_{D \text{ Form}}^{Ext}(t) = \frac{1}{\rho_0 U^2 A_{front}^{proj}} \int_{y_1}^{y_2} \int_{x_1}^{x_2} -\rho_0 g \eta(x, y, t) \frac{\partial b}{\partial x} dx dy, \quad (1b)$$

$$527 \quad C_{D \text{ Form}}^{Int}(t) = \frac{1}{\rho_0 U^2 A_{front}^{proj}} \int_{y_1}^{y_2} \int_{x_1}^{x_2} -p_{int}(x, y, t) \frac{\partial b}{\partial x} dx dy, \quad (1c)$$

$$528 \quad C_{D \text{ Form}}^{Tot}(t) = C_{D \text{ Form}}^{Int}(t) + C_{D \text{ Form}}^{Ext}(t), \quad (1d)$$

529 where τ_b^x is the along-shore component of the skin bottom friction stress. The
 530 double integral is performed on the area IJKL shown in Fig. 1. Specifically
 531 $\overline{IJ} = x_2 - x_1$ and $\overline{KJ} = y_2 - y_1$.

532 The external form drag is expected to reflect all the sea surface deformations
 533 and to be associated with the eddies forming downstream of the cape over the
 534 area with slope topography. If we consider just the external contribution, lee
 535 cyclones will depress the sea surface enhancing the external pressure difference
 536 across the obstacle and increasing the form drag. For the same mechanism, an-
 537 ticyclones will elevate the surface decreasing the form drag. Given the sequence
 538 of anticyclones and cyclones, it is not exactly clear what the net external form
 539 drag will be in the case of eddy shedding.

540 The internal form drag, instead, is expected to be connected with the deep-
 541 ening of the isopycnals behind the ridge of the obstacle. This effect is usually
 542 due to the formation of lee waves (MacCready and Pawlak, 2001), but it can
 543 be also associated with the internal density structure of the eddies formed and
 544 shed. Also in this case, it is not clear what the net internal form drag will be
 545 when lee waves and different eddies coexist.

546 Fig. 10 shows the different drag coefficients calculated according to equations
 547 (1) for the $\alpha = 0.01$ case and different Bu . In all cases the total form drag
 548 has the expected positive sign, i.e. it is directed opposite to the incoming
 549 current and it is much larger than the skin drag. A closer look at $C_{D \text{ Fric}}^{Eff}$
 550 reveals that this latter is always $\mathcal{O}(10^{-3})$, while for the $\alpha = 0.01$ slope, the
 551 total form drag coefficient is always at least two orders of magnitude larger.
 552 When $Bu = 0.05$ we know that no separation occurs. Thus, the external and
 553 the internal drags are both positive and stationary in time after an initial
 554 transient adjustment (Fig. 10a). Their addition results in a more positive
 555 total form drag. When $Bu = 1.00$, instead, external and internal drags are

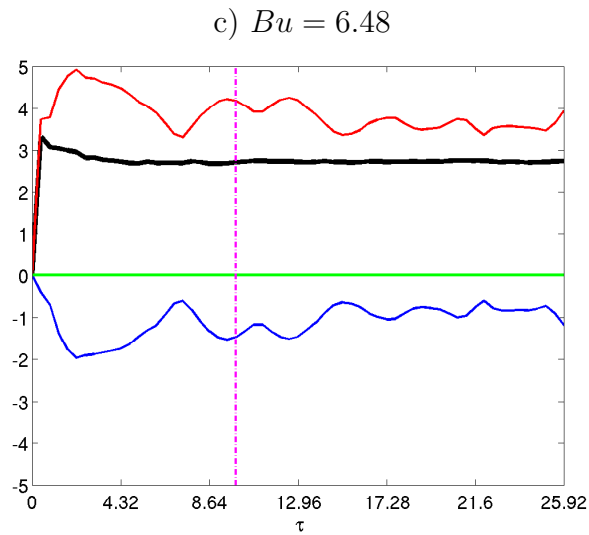
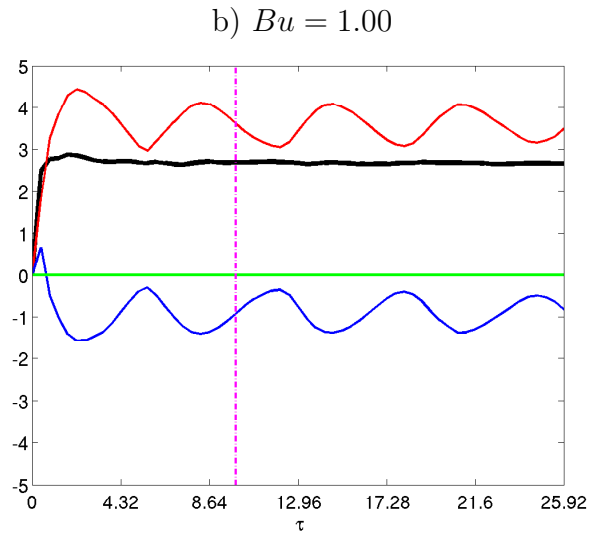
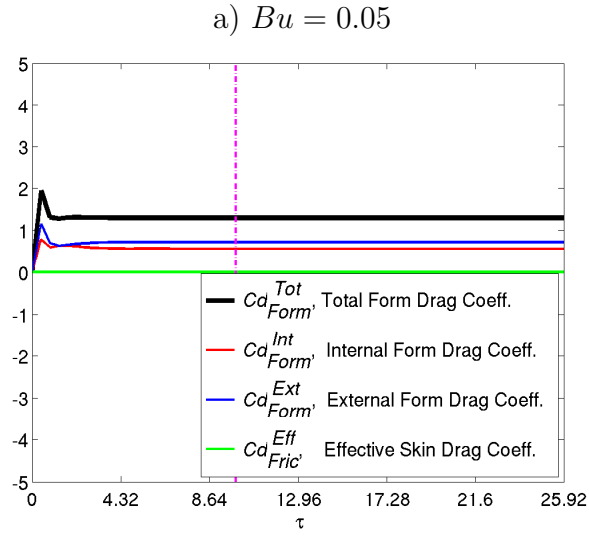


Fig. 10. Drag coefficients in time for the $\alpha = 0.01$ simulations. The magenta dot-dashed vertical line indicates the specific time for Fig. 12.

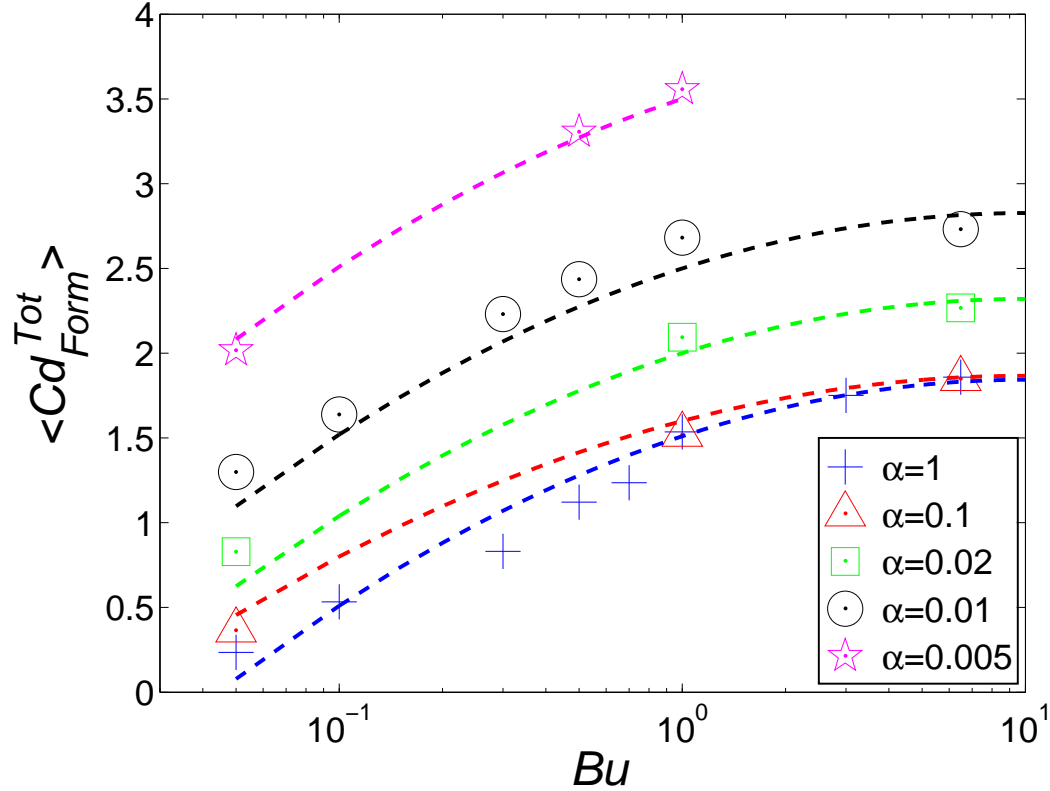


Fig. 11. Total Drag coefficients as a function of Bu and α . Symbols refer to experiments and dashed lines are from equation (2). Note that the x -axis is logarithmic.

antisymmetric and regularly oscillating in time (Fig. 10b). The net result of such an asymmetry is a compensation which reduces the time variability of total form drag keeping it almost constant for all the simulated times (Fig. 10b). When $Bu = 6.48$, the form drags oscillate less regularly (Fig. 10c). They are always antisymmetric but larger than before. For this reason, the total form drag reaches a slightly more positive value than for $Bu = 1.00$.

Since the total form drag remains nearly constant after a short adjustment, we calculate a time average total form drag coefficient $\langle C_{D Form}^{Tot} \rangle$ for all the simulations. We decide to start from $\tau = 4.32$ in order to exclude the transient adjustment period. In Fig. 11 the averaged total form drag coefficient $\langle C_{D Form}^{Tot} \rangle$ is reported on a semi-logarithmic plot in function of the Burger number and for different slopes. If we start the analysis with the $\alpha = 1$ runs (blue crosses), we can see how the total amount of energy extracted from the large scale flow is clearly a function of the stratification. On a semi-logarithmic plot, such an increase is almost linear for small and intermediate Burger numbers, while it seems to slightly flatten out for higher Bu . The amount of energy extracted in the strongly stratified cases is much larger. For example, the total

577 form drag coefficients for $Bu = 6.48$ is ≈ 1.75 , i.e. almost seven times bigger
578 than the $Bu = 0.05$ case (≈ 0.25). The same trend is found for different slopes:
579 the total form drag always increases with Bu , for constant slopes. A general
580 tendency to have flatter curves for high values of Bu can also be observed for
581 gentler cases. However, the same coefficients are also systematically higher for
582 decreasing slopes. This happens for all Bu and represents a surprising result,
583 since the increase in drag moving toward gentler slopes is comparable to the
584 one due to stronger stratification. For $Bu = 0.05$, for example, the total form
585 drag coefficient for the $\alpha = 0.005$ case is ≈ 2 , i.e. eight times bigger than for
586 the $\alpha = 1$ case.

587 In order to derive a function able to parameterize the loss of momentum due to
588 unresolved cape-like features in future coarse simulations, we fit empirically the
589 dependency of the averaged total form drag coefficient on the Burger number
590 and on the slope α . For this purpose, the following second order logarithmic
591 polynomial is proposed:

$$592 \quad \langle C_{D_{Form}}^{Tot} \rangle (Bu, \alpha) = c_2(\alpha) \log^2(Bu) + c_1(\alpha) \log(Bu) + c_0(\alpha), \quad (2)$$

593 where, if $m = 1/100$ and $q = 1.5$, the slope dependent constants are defined
594 as:

$$595 \quad c_0(\alpha) = \frac{m}{\alpha} + q,$$

$$596 \quad c_1(\alpha) = -2c_2,$$

$$597 \quad c_2(\alpha) = - \left| \frac{1 - 2\alpha}{3} \right|.$$

599 In Fig. 11 we graph with dashed lines the curves obtained using equation (2) for
600 different Burger numbers and slopes. Fig. 11 and equation (2) empirically show
601 that the coastal flow experiences a larger drag for more stratified flows over
602 gentler obstacles, but they do not explain what are the physical mechanisms
603 behind this behavior. In particular we have to understand the reasons for:

- 604 • the oscillating antisymmetric patterns for external and internal form drags;
- 605 • the increase of the form drag for higher Bu , no matter what slope is con-
- 606 sidered;
- 607 • the increase of the form drag for gentler slopes, either for small or high Bu .

608 Let us consider five different quantities defined as

$$609 \quad I(x, y, t) = \begin{cases} p_{int}(x, y, t) - p_{int}(x, y, t = 0) & \text{if } \frac{\partial b}{\partial x} \neq 0, \\ 0 & \text{if } \frac{\partial b}{\partial x} = 0, \end{cases} \quad (3)$$

$$610 \quad E(x, y, t) = \begin{cases} \eta(x, y, t) & \text{if } \frac{\partial b}{\partial x} \neq 0, \\ 0 & \text{if } \frac{\partial b}{\partial x} = 0, \end{cases} \quad (4)$$

$$611 \quad S_I(y, t) = \frac{y_2 - y_1}{\rho_0 U^2 A_{front}^{proj}} \int_{x_1}^{x_2} -p_{int}(x, y, t) \frac{\partial b}{\partial x} dx, \quad (5)$$

$$612 \quad S_E(y, t) = \frac{y_2 - y_1}{\rho_0 U^2 A_{front}^{proj}} \int_{x_1}^{x_2} -\rho_0 g \eta(x, y, t) \frac{\partial b}{\partial x} dx, \quad (6)$$

$$613 \quad S_T(y, t) = S_I(y, t) + S_E(y, t). \quad (7)$$

614 The quantity I is the internal pressure field on the sea bottom subtracted at
615 any time by the initial pressure and masked for null slope regions. Because of
616 the along-stream symmetry of the obstacle in our simulations, the simultane-
617 ous presence of upstream positive and downstream negative anomalies is an
618 indication of higher positive values for the internal form drag. The quantity
619 E , instead, just masks the sea surface heights for null slope grid points and
620 the differences across the obstacle of this quantity lead to different values for
621 the external form drag. This difference reflects the variations of the sea surface
622 for different mechanisms including the presence of different eddies in the lee
623 of the cape. The quantities S_I and S_E sum up all the along-shore contribu-
624 tions to the internal and external form drag coefficients, respectively. S_T
625 is just their net. They indicate where $C_{D\ Form}^{Int}$ and $C_{D\ Form}^{Ext}$ assume high values in
626 the cross-stream direction. Looking at I , E , S_T , S_I and S_E , we can basically
627 establish where the highest contributions to the total, internal and external
628 form drags take place.

629 Fig. 12 shows the plan view of I and E and the integrated quantities S_T
630 (black thin line), S_I (red line) and S_E (blue line) for the same simulations
631 of Fig. 10, i.e. for $\alpha = 0.01$ and for different Bu . In all the plots $\tau = 9.936$
632 and the quantities reflect the situation of the vorticity fields shown in Fig.
633 6. Since we already know that the total form drag remains almost constant
634 in time, the situation pictured in Fig. 12 can provide useful indications for
635 the whole simulated time. The increase of the total form drag for higher Bu
636 when α is kept constant reflects the role of stratification in enhancing hori-
637 zontal movements and in favoring flow separation. When no separation occurs
638 (Fig. 12a), both the internal pressure and the sea surface fields remain almost
639 symmetric across the obstacle and the total form drag is positive but small.

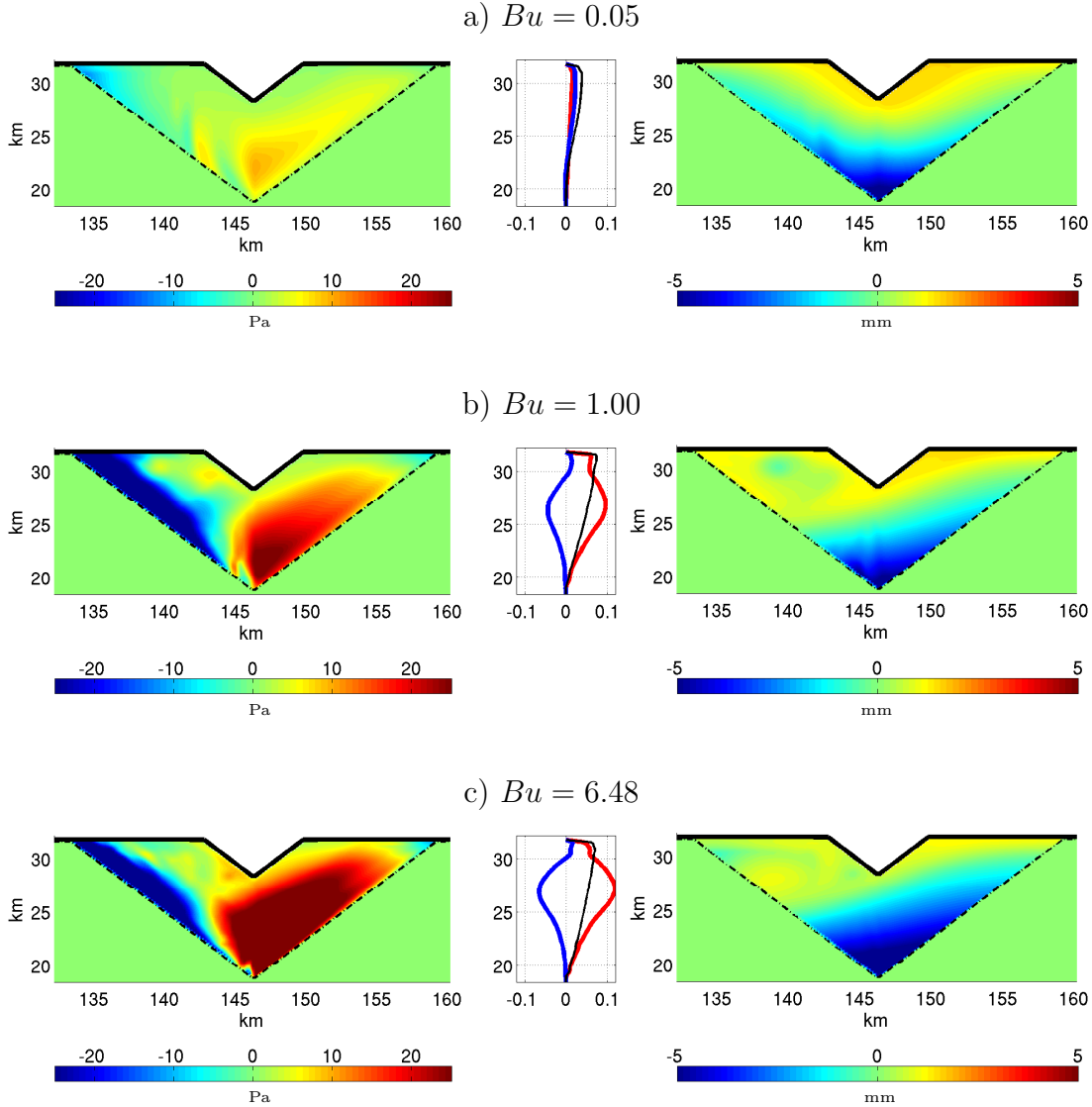


Fig. 12. Left panels: plan view of the quantity I . Center panels: the non-dimensional along-shore integrated quantities S_T (black thin line), S_I (red line) and S_E (blue line) as a function of the across-shore direction. Right panels: plan view of the quantity E . In all the plots $\alpha = 0.01$, $\tau = 9.936$ and the dash-dotted line indicates where the slope ends.

645 For increasing Bu (Fig. 12b), the separation process represents the common
 646 physical phenomenon leading to two diametrically opposite effects. It elevates
 647 the sea surface and depresses the isopycnals in the lee of the cape. This explain
 648 the clear antisymmetric temporal trends for internal and external drags. The
 649 level of the total drag is decided by the net of the two. When $Bu = 6.48$, the
 650 separation process is stronger and the drags are larger in magnitude but still

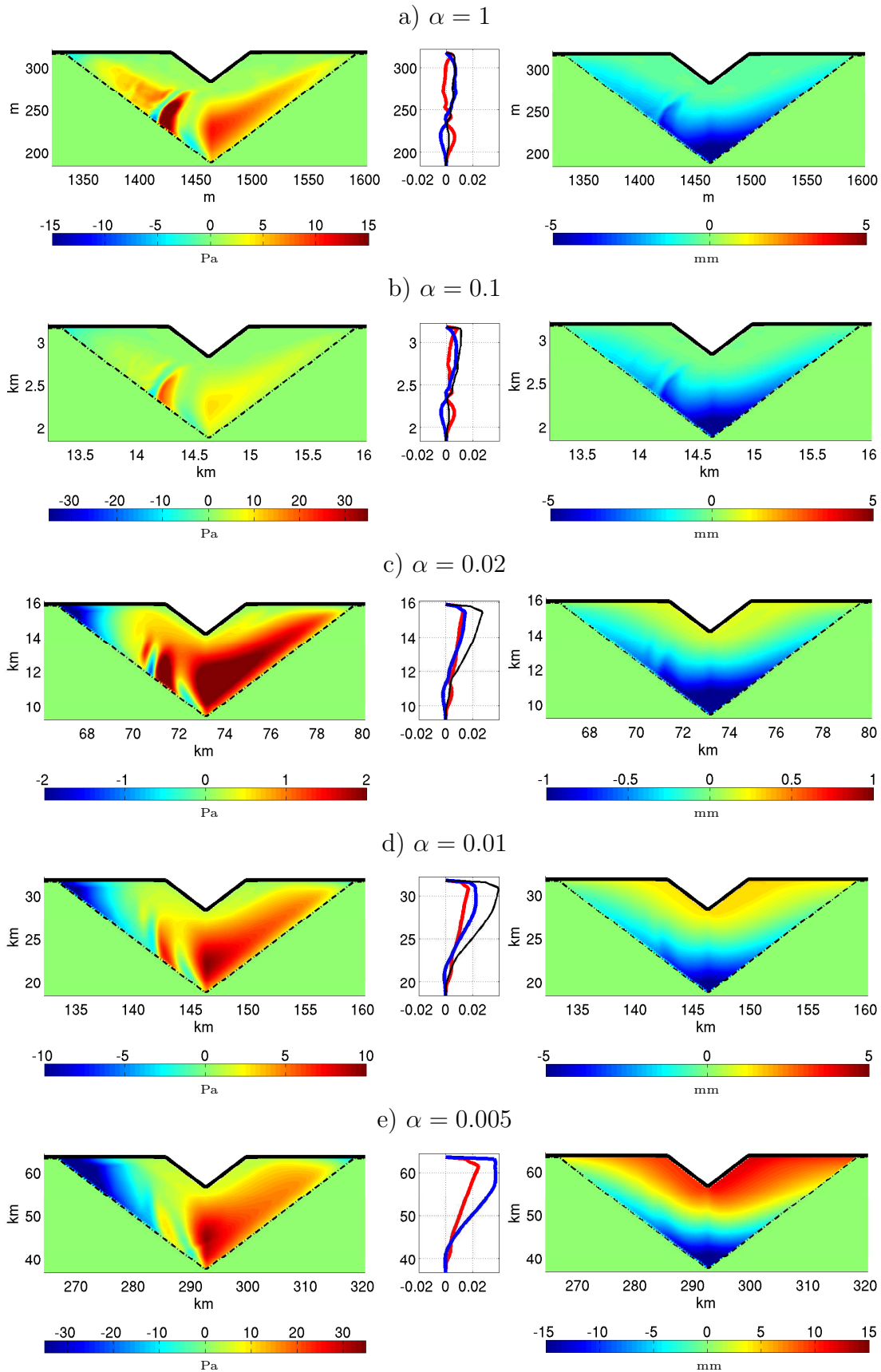


Fig. 13. As in Fig. 12 but for $Bu = 0.05$ and different α .

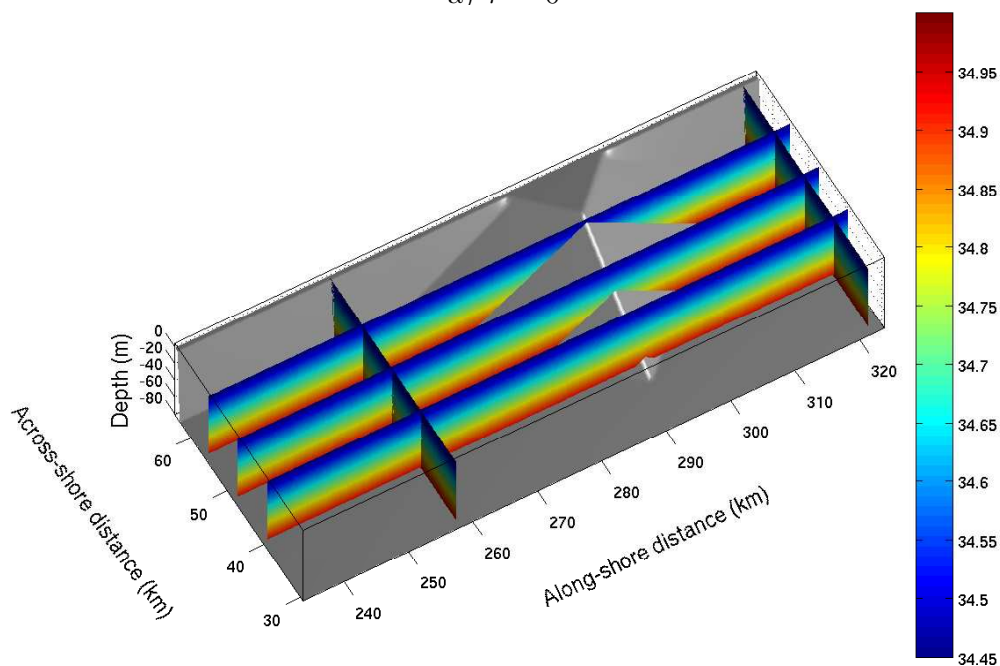
651 oppositely directed. The net drag just increases slightly. This general scenario
652 is complicated by the simultaneous surface eddy shedding regime at surface.
653 When surface cyclones are formed (Fig. 12b), the sea surface locally depresses
654 and the external form drag is less negative. Meanwhile the internal pressure
655 difference and the internal form drag decrease. Viceversa for surface anticy-
656 clones. The eddies shedding at the surface are therefore responsible for the
657 oscillations in the drags observed in time in Fig. 10b and 10c.

658 We now investigate the mechanism behind the increasing drag with gentler
659 slopes. Since the separation process takes places also at intermediate or high
660 Bu , it is likely that an explanation similar to the previous case can be found.
661 Indeed, negative internal pressure areas appear downstream the obstacle and
662 gradually increase in size for the gentler cases (not shown). Their preferential
663 orientation is parallel to the obstacle baseline as before. We already know from
664 the previous paragraph that in gentler cases larger eddies form and they are
665 proportionally more in contact with the bottom than for steeper obstacles.
666 Boundary layer mixing is therefore larger for decreasing slopes and the pres-
667 ence of lighter waters justifies the negative pressure anomalies downstream of
668 the cape.

669 We still need to explain the mechanisms behind the increasing drag with
670 gentler slopes for low Bu . In these cases, separation is not observed and the
671 previous arguments do not work. Since all the simulations run at $Bu = 0.05$
672 reach quickly a steady state, the situation depicted in the following figures for
673 $\tau = 9.936$ is representative of the whole simulation. Fig. 13 shows that negative
674 internal pressure anomalies located in the area closer to the shore become
675 gradually more important for gentler slope cases and are responsible for the
676 increase of the internal form drag. Note that their preferential orientation is
677 perpendicular to the obstacle baseline and not parallel as before. At the same
678 time, a lee depression in the surface height located in the near-shore lee of
679 the cape is responsible for the increase of the external form drag. Contrarily
680 to what happens for larger Bu , the external form drag is now positive and it
681 sums up with the internal for larger total drags values. In the last plot S_T is
682 so big as to be off-scale.

683 In order to find a phenomenon able to explain the simultaneous appearance
684 of lighter water and surface depression in the lee of the cape, we also plot a
685 three-dimensional view of the salinity field in the $\alpha = 0.005$ case (Fig. 14). The
686 initial condition is symmetric across the cape and does not result in a drag
687 (Fig. 14a). However, if we look at the same field later on, the situation changes
688 drastically. Near the coastline downstream of the cape, saltier waters are not
689 present anymore. It is evident that the presence of lighter waters is linked to
690 the increase in the ridge height moving toward the coast. Saltier waters are
691 still retained offshore when the obstacle height is small but they gradually
692 disappear close to the coast for increasing obstacle heights (Fig. 14b).

a) $\tau = 0$



b) $\tau = 9.936$

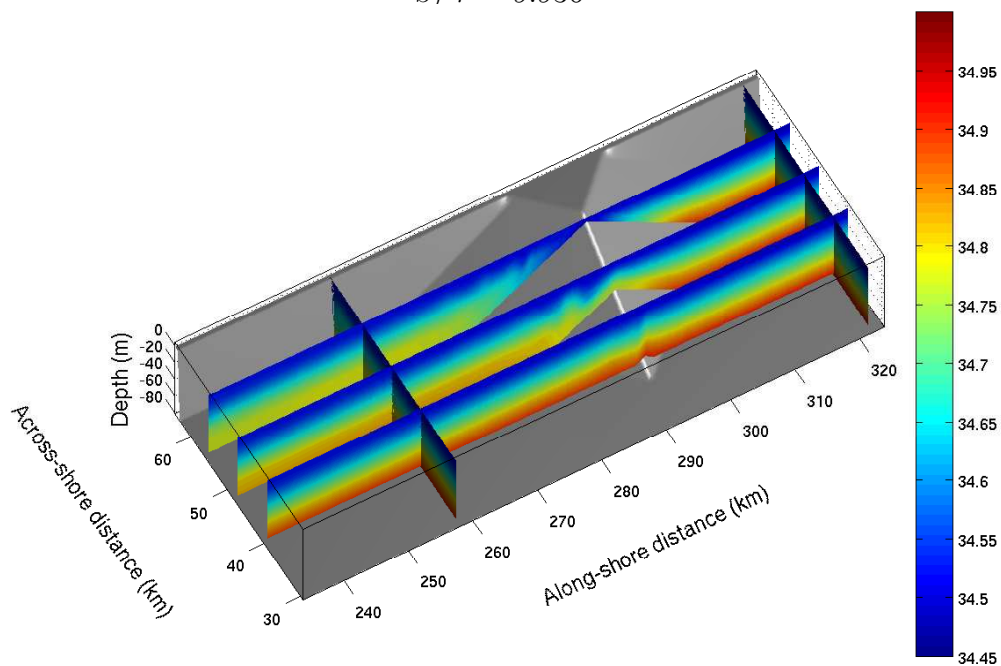


Fig. 14. Three-dimensional close up of the salinity field at different times for the case when $Bu = 0.05$ and $\alpha = 0.005$.

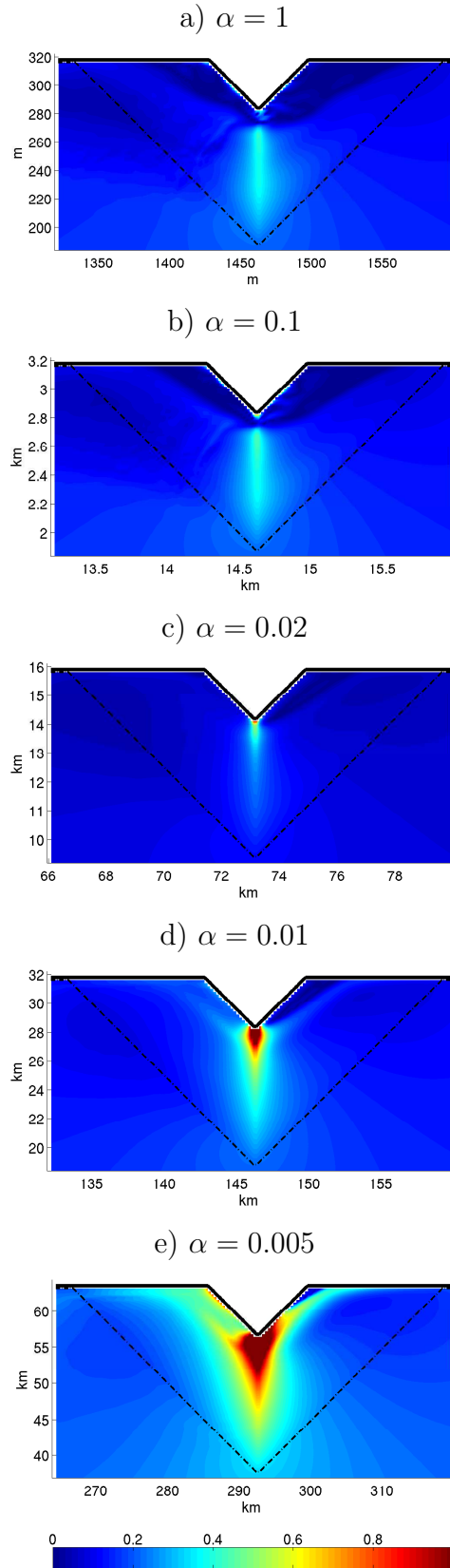


Fig. 15. Plan views of the local internal Froude numbers for the simulations with $Bu = 0.05$ and different α . In all the plots $\tau = 9.936$ and the dotted line indicates where the slope ends.

693 All the evidence collected so far suggests that the low Bu cases are dominated
 694 by hydraulic processes whose importance increases for gentler slopes. In order
 695 to confirm this hypothesis, the local internal Froude number is calculated in
 696 each grid-point according to the relation

$$697 \quad Fr_I(x, y, t) = \frac{|\bar{u}(x, y, t)|}{\sqrt{g'(x, y, t) h(x, y, t)}}, \quad (8)$$

698 where \bar{u} is the along-shore component of the vertically averaged velocity, h
 699 is the depth and $g' = g(\rho_{bot} - \rho_{surf})/\rho_0$ is the reduced gravity in each grid-
 700 point. ρ_{bot} and ρ_{surf} are the density values at the bottom and at the surface,
 701 respectively. Plan views of Fr_I for all the $Bu = 0.05$ cases are shown in Fig.
 702 15 for different slopes. Fr_I reaches the maximum in all the simulations at the
 703 crest of the ridge. The gentler cases are characterized by areas where the flow
 704 is locally supercritical ($Fr_I \geq 1$). The extension of these areas increases for
 705 decreasing slopes and leads to a larger downstream mixing associated with
 706 hydraulic jumps. This mixing, the deepening of the sea surface height and of
 707 the isopycnals, all result in less bottom pressure on the lee-side of the cape
 708 and in a larger form drag.

709 4 Summary and concluding remarks

710 We present a numerical study aimed to assess under which conditions different
 711 flow regimes occur behind a costal cape. We initially model after the laboratory
 712 experiments by Boyer and Tao (1987). As in the laboratory, we observe that
 713 the regimes strongly depend on the Burger number Bu . For strongly stratified
 714 waters, Bu increases and horizontal movements are favored with respect to
 715 vertical ones. As a consequence, eddy separation is more likely to occur than
 716 lee wave generation and we pass from a fully-attached regime, to tip eddies,
 717 followed by a lee eddy shedding regime. For high Bu the lee shedding become
 718 stronger and more evident. The eddy-attached regime observed by Boyer and
 719 Tao (1987) for intermediate Bu is not reproduced in our simulations. We raise
 720 the possibility that this regime could be a very transient one, limited to a small
 721 parameter range between the fully-attached and the eddy shedding. Its relative
 722 importance in the laboratory experiments can be attributed to features that
 723 cannot be reproduced in our runs.

724 The extension of the case study by Boyer and Tao (1987) to gentler and more
 725 realistic slopes reveals the competitive role of bottom friction. Bottom friction
 726 quickly damps and spins down turbulent structures while stratification tends
 727 to increase the two-dimensionality of the flow and to confine the damping role
 728 just to the deeper layers. For decreasing slopes, the surface lee eddy shedding
 729 regime is gradually reached at higher Bu . For the gentler cases and for in-

730 intermediate Bu , the regime is replaced by just tip eddies. At the bottom, the
731 strong lee eddy shedding is weakened for intermediate slope. For gentler cases,
732 bottom friction becomes so important as to slow down the eddy formation.
733 It can spin down the first eddy forming in the lee (eddy-attached regime) or
734 to inhibit completely its formation. In the latter case, only tip eddies can be
735 observed. Flow diagram regimes summarizing these results are presented. Fi-
736 nally, when the lee eddy shedding regime is established, the Strouhal number
737 is shown to decrease with the Burger number.

738 Even if bottom friction plays a key role in setting up the flow regimes behind
739 the cape, the quantification of the form drag coefficients in all the simulations
740 shows that these latter are at least $\mathcal{O}(10^{-1})$, i.e. 100 times bigger than the skin
741 drag ones. This result is consistent with previous works recognizing the form
742 drag as the principal mechanism for the loss of momentum in a coastal flow
743 (Moum and Nash, 2000; MacCready and Pawlak, 2001; Klymak and Gregg,
744 2004).

745 In order to understand which physical processes are responsible of the form
746 drag values, we tell apart the two different contributions due to sea surface
747 anomalies and to isopycnal deformations. The internal and external form drag
748 coefficients are calculated separately and then summed up. We found that
749 in weakly stratified non-eddy regimes, the internal and external form drags
750 are due to internal waves and both are positive. When the flow is subcritical
751 (steep cases), their values are small, but in the presence of supercritical flows
752 with hydraulic jumps (gentle cases), the downstream mixing, the deepening
753 of the isopycnals and of the sea surface are so substantial as to result in
754 larger drag values. When the stratification increases, the external form drag
755 is positive and it opposes the deceleration of the flow. This is due to the
756 predominant presence of positive sea surface anomalies associated with the
757 separation process behind the cape. The respective internal structure, however,
758 leads to the opposite effect for the internal pressure at the bottom. As a result,
759 the internal form drag shows an antisymmetric temporal trend relative to the
760 external drag, and it is able to overcome the latter. The increasing tendency
761 for flow separation and eddy generation for higher Bu and gentler slopes sets
762 up the mean level drag values and leads to larger form drag coefficients. The
763 surface eddy shedding is merely responsible for the oscillating time pattern
764 around this level.

765 The results presented, therefore, provide useful insights for future and more
766 realistic modeling. Here we underline how the form drags strongly depends on
767 the flow regimes and on the physical processes established in different condi-
768 tions. Moreover, the scientific literature already recognizes the importance of
769 the form drag in explaining strong additional dissipation in coastal areas rich
770 with topographic features (Lavelle et al., 1988; Foreman et al., 1995; Edwards
771 et al., 2004). In order to simulate the effects of unresolved capes in future

772 simulations, we put forth an empirical fit to the form drag coefficient in the
 773 $Bu - \alpha$ space based on the numerical experiments. The proposed function
 774 can be employed as a parametrization of form drag associated with flows past
 775 unresolved capes in coarse resolution simulations.

776 This study has also implications for the transport of pollutants, sediments and
 777 biological substances. The results indicate that larger particle trapping by the
 778 eddies and consequent dispersion when they shed, are phenomena likely to
 779 occur for steeper capes and in summertime, when waters are less affected by
 780 bottom friction and more stratified. At the same time, for the gentler cases,
 781 this study shows that horizontal dispersion at the bottom is strongly reduced
 782 when the eddy-attached regime occurs. If a pollutant source is located at
 783 depth in the lee of the cape (e.g. sewage pipes), these results suggest that
 784 anoxic conditions are likely to occur.

785 However, the conclusions of the study are strongly related to the geometry of
 786 the cape. Its horizontal dimension, its slope and the shape of the submerged
 787 ridge are shown to influence the results throughout the paper. The actual
 788 generalization of the phenomena here described is not yet assessed at this
 789 stage. There are many effects that can contribute to alter the flow dynamics
 790 and the form drag, such as the variability of the incoming current (Aiken
 791 et al., 2002) or the direction and the strength of a blowing wind (Winant,
 792 2006). Further investigations in terms of both numerical modeling and field
 793 measurements are necessary to assess all these points.

794 A Classification of flow regimes

795 The time evolution of the ratio KE/KE_0 can be used to classify the different
 796 flow regimes in the numerical runs.

797 Tables A.1 and A.2 collect the trend types and the temporal standard devia-
 798 tions σ for each simulation at surface and at the bottom, respectively. For the
 799 calculation of σ , we start from $\tau = 4.32$ to exclude the initial transient adjust-
 800 ment period. The flow regimes are assigned according to the type of trend and
 801 the value of σ . The type of trend is looked first. If it is an oscillating regime,
 802 the value of the standard deviation is considered. Specifically:

- 803 • if $\sigma \leq 3 \times 10^{-2}$ \mapsto Tip eddies regime;
- 804 • if $3 \times 10^{-2} < \sigma \leq 1 \times 10^{-1}$ \mapsto Lee eddy shedding regime;
- 805 • if $\sigma > 1 \times 10^{-1}$ \mapsto Strong lee eddy shedding regime.

806 If it is a decaying trend, a second decision is taken based on σ . If $\sigma > 1 \times 10^{-1}$
 807 the strong energetic shedding is just weakened, while if $\sigma \leq 1 \times 10^{-1}$, an

<i>Surface</i>					
Exp.	Slope (α)	Bu	Trend	σ	Regime
2	1	0.05	Steady	3.50×10^{-3}	Fully-attached
3	1	0.10	Oscillating	7.00×10^{-3}	Tip eddies
4	1	0.30	Oscillating	1.87×10^{-2}	Tip eddies
5	1	0.50	Oscillating	7.35×10^{-2}	Eddy shedding
6	1	0.70	Oscillating	6.67×10^{-2}	Eddy shedding
7	1	1.00	Oscillating	8.78×10^{-2}	Eddy shedding
8	1	3.00	Oscillating	1.54×10^{-1}	Strong eddy shedding
9	1	6.48	Oscillating	1.30×10^{-1}	Strong eddy shedding
10	0.1	0.05	Steady	2.22×10^{-3}	Fully-attached
11	0.1	1.00	Oscillating	6.17×10^{-2}	Eddy shedding
12	0.1	6.48	Oscillating	1.65×10^{-1}	Strong eddy shedding
13	0.02	0.05	Steady	3.61×10^{-4}	Fully-attached
14	0.02	1.00	Oscillating	7.20×10^{-2}	Eddy shedding
15	0.02	6.48	Oscillating	2.61×10^{-1}	Strong eddy shedding
16	0.01	0.05	Steady	1.85×10^{-4}	Fully-attached
17	0.01	0.10	Steady	9.02×10^{-5}	Fully-attached
18	0.01	0.30	Oscillating	1.29×10^{-2}	Tip eddies
19	0.01	0.50	Oscillating	1.47×10^{-2}	Tip eddies
20	0.01	1.00	Oscillating	4.89×10^{-2}	Eddy shedding
21	0.01	6.48	Oscillating	1.47×10^{-1}	Strong eddy shedding
22	0.005	0.05	Steady	1.58×10^{-4}	Fully-attached
23	0.005	0.50	Oscillating	6.85×10^{-3}	Tip eddies
24	0.005	1.00	Oscillating	3.92×10^{-2}	Eddy shedding

Table A.1
Classification of surface flow regimes for all the simulations.

<i>Bottom</i>					
Exp.	Slope (α)	Bu	Trend	σ	Regime
2	1	0.05	Steady	4.49×10^{-3}	Fully-attached
3	1	0.10	Oscillating	8.75×10^{-3}	Tip eddies
4	1	0.30	Oscillating	5.19×10^{-2}	Eddy shedding
5	1	0.50	Oscillating	1.11×10^{-1}	Strong eddy shedding
6	1	0.70	Oscillating	1.90×10^{-1}	Strong eddy shedding
7	1	1.00	Oscillating	2.15×10^{-1}	Strong eddy shedding
8	1	3.00	Oscillating	4.71×10^{-1}	Strong eddy shedding
9	1	6.48	Oscillating	5.11×10^{-1}	Strong eddy shedding
10	0.1	0.05	Steady	3.34×10^{-3}	Fully-attached
11	0.1	1.00	Decaying	1.63×10^{-1}	Eddy shedding
12	0.1	6.48	Decaying	2.86×10^{-1}	Eddy shedding
13	0.02	0.05	Steady	1.03×10^{-4}	Fully-attached
14	0.02	1.00	Decaying	3.20×10^{-2}	Eddy-attached
15	0.02	6.48	Decaying	5.91×10^{-2}	Eddy-attached
16	0.01	0.05	Steady	8.10×10^{-5}	Fully-attached
17	0.01	0.10	Steady	1.62×10^{-4}	Fully-attached
18	0.01	0.30	Oscillating	7.19×10^{-3}	Tip eddies
19	0.01	0.50	Oscillating	1.48×10^{-2}	Tip eddies
20	0.01	1.00	Oscillating	1.25×10^{-2}	Tip eddies
21	0.01	6.48	Decaying	5.83×10^{-2}	Eddy-attached
22	0.005	0.05	Steady	4.56×10^{-5}	Fully-attached
23	0.005	0.50	Oscillating	3.14×10^{-3}	Tip eddies
24	0.005	1.00	Oscillating	6.30×10^{-3}	Tip eddies

Table A.2
Classification of bottom flow regimes for all the simulations.

808 eddy-attached regime is assigned. Finally, if it is a flat and steady trend, a
809 fully-attached regime is assigned.

810 The information contained in Tables A.1 and A.2 are displayed in the already
811 proposed Fig. 8.

812 References

- 813 Aiken, C. M., Moore, A. M., Middleton, J. H., 2002. The nonnormality of
814 coastal ocean flows around obstacles and their response to stochastic forcing.
815 *J. Mar. Sys.* 32 (10), 2955–2974.
- 816 Alaei, M. J., Ivey, G., Pattiaratchi, C., 2004. Secondary circulation induced
817 by flow curvature and Coriolis effects around headlands and islands. *Ocean*
818 *Dynamics* 54, 27–38, doi:10.1007/s10236-003-0058-3.
- 819 Baines, P. G., 1995. *Topographic Effects in Stratified Flows*. Cambridge Uni-
820 versity Press.
- 821 Bastos, A., Collins, M., Kenyon, N., 2003. Water and sediment movement
822 around a coastal headland: Portland Bill, Southern UK. *Ocean Dynamics*
823 53 (3), 309–321.
- 824 Bastos, A., Kenyon, N., Collins, M., 2002. Sedimentary processes, bedforms
825 and facies, associated with a coastal headland: Portland Bill, Southern UK.
826 *Mar. Geol.* 187 (3-4), 235–258.
- 827 Batchelor, G., 1967. *An Introduction to Fluid Dynamics*. Cambridge Univer-
828 sity Press.
- 829 Boyer, D., Chen, R., d’Hères, G. C., Didelle, H., 1987. On the formation and
830 shedding of vortices from side-wall mounted obstacles in rotating systems.
831 *Dyn. Atmos. Oceans* 11, 59–86.
- 832 Boyer, D., Davies, P. A., 1982. Flow past a cylinder on a β -plane. *Phil. Trans.*
833 *R. Soc. London A* 306, 33–56.
- 834 Boyer, D., Metz, M. L., 1983. Vortex shedding in rotating flows. *Geophys.*
835 *Astrophys. Fluid Dynamics* 26, 51–83.
- 836 Boyer, D., Tao, L., 1987. On the motion of linearly stratified rotating fluids
837 past capes. *J. Fluid Mech.* 180, 429–449.
- 838 Canuto, V. M., Howard, A., Cheng, Y., Dubovikov, M. S., 2001. Ocean tur-
839 bulence, Part i: one-point closure model momentum and heat vertical dif-
840 fusivities. *J. Phys. Oceanogr.* 31, 1413–1426.
- 841 Chiswell, S., Roemmich, D., 1998. The East Cape Current and two eddies: a
842 mechanism for larval retention? *N. Z. J. Mar. Freshwat. Res.* 32 (3), 385–
843 397.
- 844 Coutis, P. F., Middleton, J. H., 2002. The physical and biological impact of a
845 small island wake in the deep ocean. *Deep Sea Res. I* 49, 1341–1361.
- 846 Cushman-Roisin, B., Korotenko, K. A., Galos, C. E., Dietrich, D. E., 2007.

- 847 Simulation and characterization of the Adriatic Sea mesoscale variability.
848 *J. Geophys. Res.* 112, C03S14, doi:10.1029/2006JC003515.
- 849 Davies, P. A., Besley, P., Boyer, D. L., 1990a. An experimental study of flow
850 past a triangular cape in a linearly stratified fluid. *Dyn. Atmos. Oceans*
851 14 (6), 497–528.
- 852 Davies, P. A., Dakin, J., Falconer, R., 1995. Eddy formation behind a coastal
853 headland. *J. Coast. Res* 11 (1), 154–167.
- 854 Davies, P. A., Davis, R. G., Foster, M. R., 1990b. Flow past a cylinder in a
855 rotating stratified fluid. *Phil. Trans. R. Soc. London A* 331, 245–286.
- 856 Doglioli, A. M., Griffa, A., Magaldi, M. G., 2004a. Numerical study of a coastal
857 current on a steep slope in presence of a cape: the case of the Promontorio
858 di Portofino. *J. Geophys. Res.* 109, C12033, doi:10.1029/2004JC002422.
- 859 Doglioli, A. M., Magaldi, M. G., Vezzulli, L., Tucci, S., 2004b. Development of
860 a numerical model to study the dispersion of wastes coming from a marine
861 fish farm in the Ligurian Sea (Western Mediterranean). *Aquaculture* 231 (1-
862 4), 215–235, doi:10.1016/j.aquaculture.2003.09.030.
- 863 Dong, C., McWilliams, J. C., Shchepetkin, A. F., 2007. Island wakes in deep
864 water. *J. Phys. Oceanogr.* 37, 962–981, doi:10.1175/JPO3047.1.
- 865 Edwards, K. A., MacCready, P., Moum, J. N., Pawlak, G., 2004. Form drag
866 and mixing due to tidal flow past a sharp point. *J. Phys. Oceanogr.* 34,
867 1297–1312.
- 868 Farmer, R., Pawlowicz, D., Jiang, R., 2002. Tilting separation flows: a mech-
869 anism for intense vertical mixing in the coastal ocean. *Dyn. Atmos. Oceans*
870 36, 43–58.
- 871 Foreman, M. G. G., Walters, R. A., Henry, R. F., Keller, C. P., Dolling, A. G.,
872 1995. A tidal model for eastern Juan de Fuca Strait and the southern Strait
873 of Georgia. *J. Geophys. Res.* 100 (C1), 721–740.
- 874 Freeland, H., 1990. The flow of a coastal current past a blunt headland.
875 *Atmosphere-Ocean* 28, 288–302.
- 876 Geyer, W. R., 1993. Three-dimensional tidal flow around headlands. *J. Geo-
877 phys. Res.* 98 (C1), 955–966.
- 878 Hayward, T. L., Mantyla, A. W., 1990. Physical, chemical and biological struc-
879 ture of a coastal eddy near Cape Mendocino. *J. Mar. Res.* 48, 825–850.
- 880 Heywood, K. J., Stevens, D. P., Bigg, G. R., 1996. Eddy formation behind the
881 tropical island of Aldabra. *Deep Sea Res. I* 43 (4), 555–578.
- 882 John, M. A. S., Pond, S., 1992. Tidal plume generation around a promontory:
883 effects on nutrient concentrations and primary productivity. *Cont. Shelf
884 Res.* 12 (2-3), 339–354.
- 885 Jones, O. P., Simons, R. R., Jones, E. J. W., Harris, J. M., 2006. Influence
886 of seabed slope and Coriolis effects on the development of sandbanks near
887 headlands. *J. Geophys. Res.* 111, C03020, doi:10.1029/2005JC002944.
- 888 Kalkwijk, J., Booij, R., 1986. Adaptation of secondary flow in nearly-
889 horizontal flow. *J. Hydraul. Eng.* 24, 19–37.
- 890 Klinger, B. A., 1993. Gyre formation at the corner by rotating barotropic
891 coastal flows along a slope. *Dyn. Atmos. Oceans* 19, 27–64.

- 892 Klymak, J. M., Gregg, M. C., 2001. Three-dimensional nature of flow near a
893 sill. *J. Geophys. Res.* 106 (C10), 22295–22311.
- 894 Klymak, J. M., Gregg, M. C., 2004. Tidally generated turbulence over the
895 Knight Inlet Sill. *J. Phys. Oceanogr.* 34 (5), 1135–1151.
- 896 Kundu, P. K., Cohen, I. M., 2002. *Fluid Mechanics*, 2nd Ed. Academic Press.
- 897 Lavelle, J. W., Mofjeld, H. O., Lempriere-Doggett, E., Cannon, G. A., Pashin-
898 ski, D. J., Cokelet, E. D., Lytle, L., Gill, S., 1988. A multiply-connected
899 channel model of tides and tidal currents in Puget Sound, Washington
900 and a comparison with updated observations. Technical Memorandum ERL
901 PMEL-84, NOAA, 103pp.
- 902 Lloyd, P. M., Stansby, P. K., Chen, D., 2001. Wake formation around islands in
903 oscillatory laminar shallow water flows. Part I: Experimental investigation.
904 *J. Fluid Mech.* 429, 217–238.
- 905 MacCready, P., Pawlak, G., 2001. Stratified flow along a corrugated slope:
906 separation drag and wave drag. *J. Phys. Oceanogr.* 31 (10), 2824–2839.
- 907 McCabe, R. M., MacCready, P. M., Pawlak, G., 2006. Form drag due to flow
908 separation at a headland. *J. Phys. Oceanogr.* 36 (11), 2136–2152.
- 909 Merkin, L.-O., 1980. Flow separation on a β -plane. *J. Fluid Mech.* 99, 399–
910 409.
- 911 Merkin, L.-O., Solan, A., 1979. The separation of flow past a cylinder in a
912 rotating system. *J. Fluid Mech.* 92, 381–392.
- 913 Moum, J. N., Nash, J. D., 2000. Topographically induced drag and mixing at
914 a small bank on the continental shelf. *J. Phys. Oceanogr.* 35 (8), 2049–2054.
- 915 Murdoch, R. C., 1989. The effects of a headland eddy on surface macro-
916 zooplankton assemblages north of Ontago Peninsula, New Zealand. *Estuar.
917 Coast. Shelf S.* 29, 361–383.
- 918 Nash, J. D., Moum, J. N., 2001. Internal hydraulic flows on the continental
919 shelf: high drag states over a small bank. *J. Geophys. Res.* 106 (C3), 4593–
920 4611.
- 921 Neill, S. P., Elliott, A. J., 2004. Observations and simulations of an unsteady
922 island wake in the Firth of Forth, Scotland. *Ocean Dynamics* 54, 324–332.
- 923 Page, M. A., 1985. On the low Rossby number flow of a rotating fluid past a
924 cylinder. *J. Fluid Mech.* 156, 205–211.
- 925 Pattiaratchi, C., James, A., Collins, M., 1986. Island wakes and headland
926 eddies: a comparison between remotely sensed data and laboratory experi-
927 ments. *J. Geophys. Res.* 92 (C1), 783–794.
- 928 Pawlak, G., MacCready, P., Edwards, K. A., McCabe, R., 2003. Observations
929 on the evolution of tidal vorticity at a stratified deep water headland. *Geo-
930 phys. Res. Lett.* 30 (24), 2234, doi:10.1029/2001JC001234.
- 931 Pedlosky, J., 1987. *Geophysical Fluid Dynamics*, 2nd Ed. Springer-Verlag.
- 932 Pingree, R. D., 1978. The formation of the shambles and other banks by tidal
933 stirring of the seas. *J. Mar. Biol. Ass. U.K.* 58, 211–226.
- 934 Pingree, R. D., Maddock, L., 1980. The effects of bottom friction and Earth’s
935 rotation on an island’s wake. *J. Mar. Biol. Ass. U.K.* 60, 499–508.
- 936 Rankin, K. L., Mullineaux, L. S., Geyer, W. R., 1994. Transport of juvenile

- 937 gem clams (*Gemma gemma*) in a headland wake. *Estuaries* 17 (3), 655–667.
- 938 Roughan, M., Mace, J., Largier, J. L., Morgan, S. G., Fisher, J. L., Carter,
939 M. L., 2005. Subsurface recirculation and larval retention in the lee of a
940 small headland: a variation on the upwelling shadow theme. *J. Geophys.*
941 *Res.* 110, C10027, doi:10.1029/2005JC002898.
- 942 Schlichting, H., Gersten, K., 2003. *Boundary Layer Theory*. Springer-Verlag.
- 943 Shchepetkin, A. F., McWilliams, J. C., 1998. Quasi-monotone advection
944 schemes based on explicit locally adaptive dissipation. *Mon. Weather Rev.*
945 126 (6), 1541–1580.
- 946 Shchepetkin, A. F., McWilliams, J. C., 2005. The regional oceanic mod-
947 eling system (ROMS): a split-explicit, free-surface, topography-following-
948 coordinate oceanic model. *Ocean Modell.* 9 (4), 347–404.
- 949 Shchepetkin, A. F., O’Brien, J. J., 1996. A physically consistent formulation
950 of lateral friction in shallow-water equation ocean models. *Mon. Weather*
951 *Rev.* 124 (6), 1285–1300.
- 952 Signell, R., Geyer, W., 1991. Transient eddy formation around headlands. *J.*
953 *Geophys. Res.* 96 (C2), 2561–2575.
- 954 Stansby, P. K., Lloyd, P. M., 2001. Wake formation around islands in oscilla-
955 tory laminar shallow water flows. Part II: Three-dimensional boundary-layer
956 modelling. *J. Fluid Mech.* 429, 217–238.
- 957 Tansley, C., Marshall, D. P., 2001. Flow past a cylinder on a β -plane, with ap-
958 plication to Gulf Stream separation and the Antarctic Circumpolar Current.
959 *J. Phys. Oceanogr.* 31, 3274–3283.
- 960 Tomczak, M., 1988. Island wakes in deep and shallow water. *J. Geophys. Res.*
961 93 (C5), 5153–5154.
- 962 Umlauf, L., Burchard, H., 2003. A generic length-scale equation for geophysical
963 turbulence models. *J. Marine Res.* 61, 235–265.
- 964 Veneziani, M., Griffa, A., Poulain, P.-M., 2007. Historical drifter data and
965 statistical prediction of particle motion: a case study in the central Adriatic
966 Sea. *J. Atmos. Ocean. Tech.* 24, 235–254, doi:10.1175/JTECH1969.1.
- 967 Verron, J., Davies, P. A., Dakin, J. M., 1991. Quasigeostrophic flow past a
968 cape in a homogeneous fluid. *Fluid Dyn. Res.* 7, 1–21.
- 969 Walker, J. D. A., Stewartson, K., 1972. The flow past a cylinder in a rotating
970 frame. *Z. Angew. Math. Phys.* 23, 745–752.
- 971 Winant, C. D., 2006. Three-dimensional wind-driven coastal circulation past
972 a headland. *J. Phys. Oceanogr.* 36, 1430–1438.
- 973 Wolanski, E., Asaeda, T., Tanaka, A., Deleersnijder, E., 1996. Three-
974 dimensional island wakes in the field, laboratory experiments and numerical
975 models. *Cont. Shelf Res.* 16 (11), 1437–1452.
- 976 Wolanski, E., Imberger, J., Heron, M., 1984. Island wakes in shallow coastal
977 waters. *J. Geophys. Res.* 89 (C6), 10553–10569.